Rotational Friction Welding of Titanium-Zirconium-Molybdenum (TZM)

Master thesis

Submitted in fulfillment of the requirements for the degree of

Diplom-Ingenieur (DI)

to the

Technical University of Graz

by

Daniel Enzo de Pretis

0930711

Graz, April 2014

STATUTORY DECLARATION

I declare that I have authored this thesis independently, that I have not used other than the declared sources / resources and that I have explicitly marked all material which has been quoted either literally or by content from the used sources.

……..……..	……..……..
Date	Daniel de Pretis

PREFACE

First of all I am deeply grateful to my supervisor from the Institute for Materials Science and Welding (IWS), *Assoc.Prof. Dipl.-Ing. Dr.techn. Norbert Enzinger* who entrusted me with this exciting topic. I also want to thank *Ing. Nikolaus Reheis* and his team (especially *Silas Wolf*) from PLANSEE SE (Joining Technologies / Innovation Services department) for enabling and supporting this thesis. Also advices given by *Dr. Jürgen Schatte* and *DI Tobias Mrotzek* have been a great help. Special thanks are directed to *Klaus Raiser (GmbH)* for executing the friction welding experiments. Assistance provided by the laboratory staff from IWS as well as from Plansee SE was greatly appreciated. Finally, I wish to thank my parents, my friends and my girlfriend for their support and encouragement throughout my studies.

Daniel de Pretis

Abstract

In this study, the potential of rotational friction welding was investigated for the Molybdenum-alloy TZM (Titanium-Zirconium-Molybdenum). Direct-drive friction welding was carried out with tubular TZM components in the diameter range of 50 mm. The welding parameters were based on the energy input of an already existing inertia-drive friction welding process. The weld was analyzed with different test methods by means of NDE (Non destructive examination) as well as destructive testing. Visual testing displayed a proper flash formation without irregularities or cracks. Minor defects identified in the circumferential areas were detected with ultrasonic- and dye penetration test. Micro-structural investigation showed a fine grained microstructure in the welding area. The micrographs in combination with the hardness measurements reveal a visible heat-affected-zone (HAZ) width of about 6 millimeters. The tensile test results at room and elevated temperature of the successfully welded samples are characterised by a slight increase of the ultimate-tensile-strength (UTS) and a considerable decrease of the fracture elongation, compared to the base material. To sum up, one specific parameter-set for direct-drive friction welding was successfully applied on tubular TZM-components.

Table of contents

Abbreviations

A	Fracture elongation
Ag	Uniform elongation
DBTT	Ductile brittle transition temperature
DoE	Design of experiments
EDX	Energy dispersive X-ray
HAZ	Heat affected zone
HT	Hardness test
HV	Hardness Vickers
L	Length
MHC	Molybdenum-Hafnium-Carbon alloy
Mo	Chemical element molybdenum
NDE	Non destructive examination
OD	Outer diameter
PM	Powder metallurgical
PT	Penetration test
(PW)HT	(Post weld) heat treatment
R_m	Tensile strength
$R_{p0,2}$	0.2% technical elastic limit
RT	Room temperature
SEM	Scanning electron microscopy
TEM	Transmission electron microscopy
T_s	Melting temperature
TT	Tensile test
TZM	Titanium-Zirconium-Molybdenum alloy
UT	Ultrasonic test
UTS	Ultimate tensile strength
W	Chemical element wolfram (tungsten)

1 Introduction

Joining of powder-metallurgical-processed molybdenum alloys can be achieved by conventional methods, including mechanical fastening, brazing and welding. Practical feasibility of welding is already demonstrated for fusion and solid state processes [1, 2]. However, technical information about experimental welding practice is limited and fundamental understanding of main influence factors is not available.

Friction welding, as a well-established commercial process, allows welding in the solid state within the forging temperature range of parent materials. Melting does not occur, thus avoiding problems regarding solidification and distortion that occur in fusion welds. Friction welding has proofed as a cost effective weld process in particular for axial-symmetric tube/disc assemblies, even in the net shape configuration. Excellent weld properties and the ability to join a variety of weld geometries are reported in [2].

Most of the friction weld experience gained so far with TZM is related to inertia welding, which is one of the technological options for rotary friction welding. For inertia welding the kinetic energy, which is needed to generate heat between the two components to be welded, is stored in a flywheel [3]. The technological alternative which is mainly utilized in Europe is known as direct-drive friction welding, where the entire weld energy is generated continuously by an electric motor drive.

In reference to the results of previous studies [1, 3, 4] the scope of this work is to investigate the potential of direct-drive friction welding for tubular TZM components in the 50 mm diameter range. This study was enabled through the cooperation between PLANSEE SE and the Institute for Materials Science and Welding at Graz University of Technology. Direct-drive friction welding was done by Klaus Raiser GmbH [6].

2 Definition of task

The main objective of this thesis is to conduct a feasibility study for a specific friction welding process. The result of this process should be a proper weld between two thick-walled pipes. The specimen material is a molybdenum-base alloy (TZM) with increased strength and improved processability. The parameters of a similar process executed on an inertia-drive friction welding machine should serve as a basis for the estimation of the energy input into the welding interface. Related to this energy input, the parameters for the execution on the available direct-drive machine were estimated. Afterwards the weld should be analyzed with different test methods by means of NDE as well as destructive testing. This feasibility study serves as a preliminary work for a following dissertation with the focus on a systematic parameter optimization (DoE). The course of action to fulfill this task is visualized in Figure 1.

Figure 1: Course of action

3 Literature review

This chapter includes a basic description of friction welding and different friction welding methods as well as relevant influencing factors. Further, an overview of the welded material will be presented.

3.1 Fundamental characteristics of friction welding processes

In contrast to other joining methods like fusion welding (heat only) or cold joining processes like mechanical fastening or magnetic impulse welding (force only), friction welding differs by making use of force and heat ($<T_s$) to obtain a proper joint (see Figure 2).

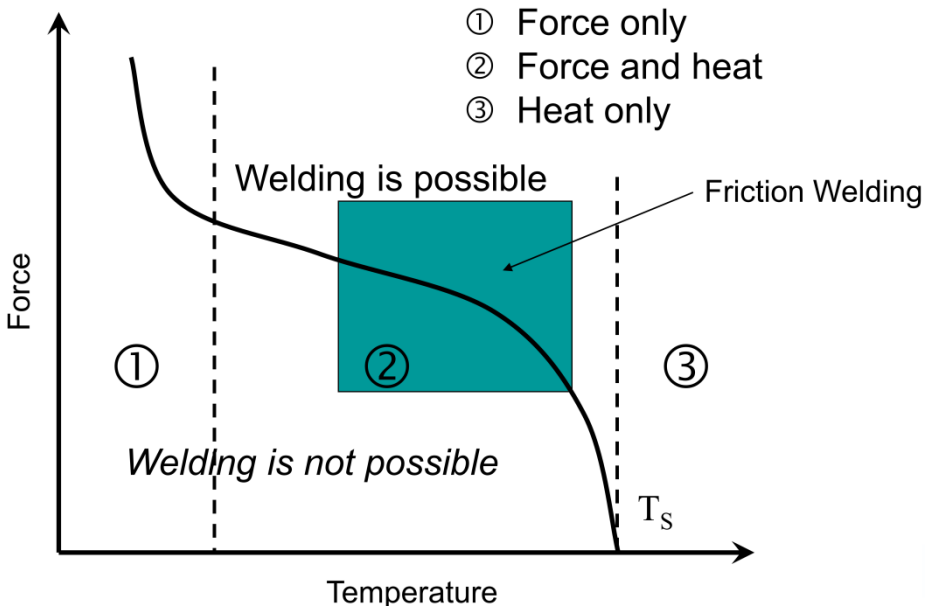

Figure 2: Principle of producing a friction welding joint (positioning of the friction welding process in relation to other joining methods) [7]

According to the American Welding Society (AWS) C6-1-89 Standard the friction welding process can be defined as follows [3]: *'Friction welding is a solid-state joining process that produces coalescence of materials under compressive force contact of workpieces rotating or moving relative to one another to produce heat and plastically displace material from the faying surfaces. Under normal conditions, the faying surfaces do not melt. Filler metal, flux and shielding gas are not required with this process'.*

3.1.1 Process variants

The basic distinction of friction welding processes is related to the type of heat generation between the parts to be welded. This heat input is produced via relative movement of the two parts which can be rotational, linear or orbital. Depending on the chosen method, the energy input in the interface can be homogenous or inhomogeneous across the area (see Figure 3). Concerning the non-uniform heat generation across the interface for rotational friction welding, a non-uniform thickness of the heat-affected-zone can be assumed. This shortcoming can be avoided by using linear and orbital friction welding where the energy input is almost uniform across the interface. [3]

The cross-section of the components is another criterion which has to be considered when choosing a friction welding method. For example, rotational friction welding cannot be used for non-circular cross-sections, whereas this is no problem in linear friction welding. [3]

In contrast to these conventional processes, other methods such as friction stir welding exist [8]. In this case the necessary heat input is generated with an additional tool and not via relative movement of the parts to be joined. However, due to the fact that this process is quite different to the scope of this work, it will not be discussed further.

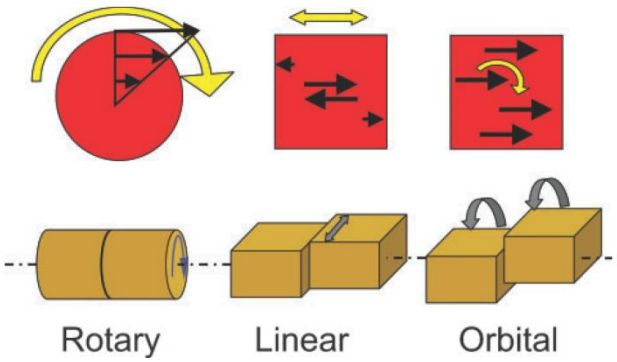

Figure 3: Three basic variants of friction welding [3]

The relevant type for this thesis is the rotational friction welding process which can be divided into three basic stages according to [3]. In the *heat-up stage* the two components are brought in contact to each other by applying an axial force together with a relative movement. Due to friction, the temperature at the interface increases, which leads to a decrease of flow stress in the material. In the *burn-off stage* the material plastically flows outwards and forms a flash which also transports oxides and contaminations out of the faying surface. Finally, the relative motion between the components stops and a high compressive force is applied to finish the weld. This is known as the *forging stage* (see Figure 4).

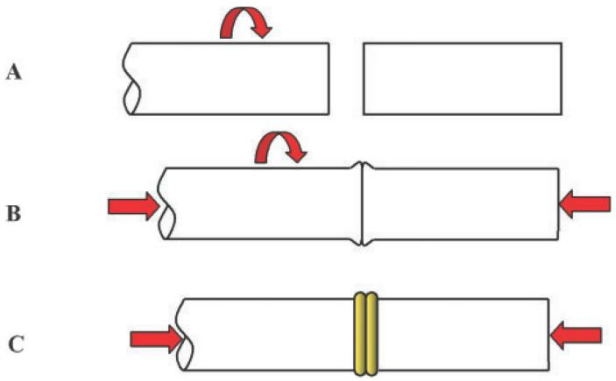

A: one specimen rotates and other is stationary; B: two specimens are brought together as axial force is applied and rubbing of faying surfaces heats specimen locally and upsetting starts; C: process is complete when rotation of one specimen stops and upsetting ceases

Figure 4: Basic steps of the rotational friction welding process [3]

Related to the way of energy conversion, rotational friction welding can be divided into direct-drive (continuous-drive) and inertia-drive friction welding.

3.1.1.1 Inertia-drive friction welding

In inertia-drive friction welding the kinetic energy which is needed to generate sufficient heat between the two components is stored in a flywheel. The three influencing process variables of this method are the mass of the flywheel, the rotational speed and the axial force. Typical curve progressions of these influencing factors can be seen in Figure 5. Unlike the direct-drive process, the rotational speed varies during the friction phase. If a constant axial force is applied, the process is called single-stage welding. If the force during the friction and the forge phase differs, it is called two-stage welding process. Due to the high energy input in a relatively

short period of time the temperature gradients are sharper in inertia-drive than in direct-drive friction welding, which results in a narrower heat-affected-zone. [3]

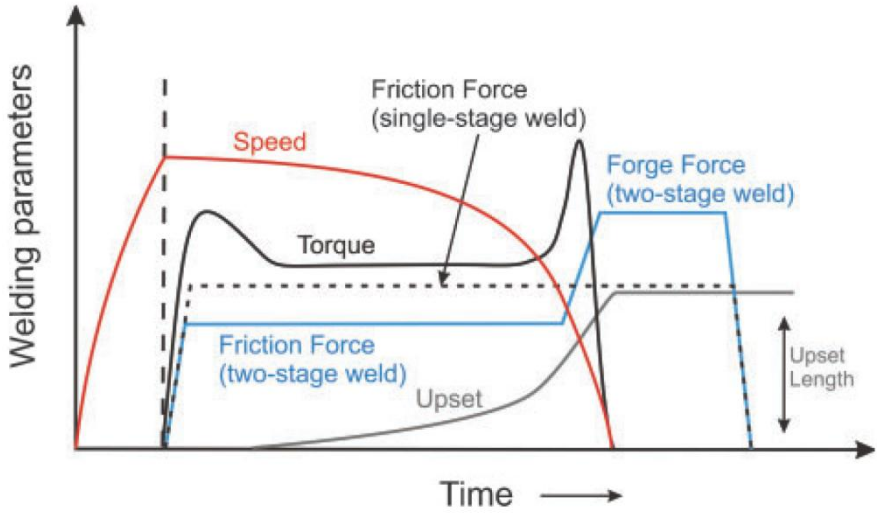

Figure 5: Welding parameters for inertia drive friction welding [3]

3.1.1.2 Direct-drive friction welding

Direct or continuous-drive friction welding – unlike inertia-drive friction welding – works without energy storage and therefore needs a constant energy source. To that end, one part is rotated by a motor while the other one stands still. After the friction phase a hydraulic cylinder applies the forge force via the static work-piece into the welding area (see Figure 6).

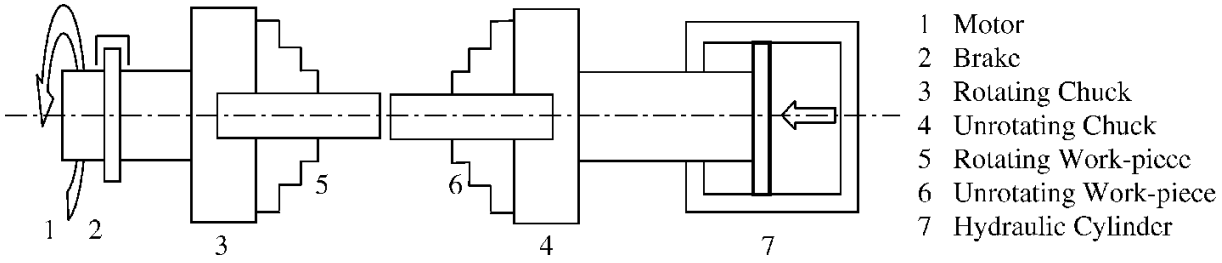

Figure 6: Layout of direct-drive friction welding [9]

The determining variables for a proper weld with this process are rotational speed, axial force and welding time. In contrast to inertia drive friction welding the rotational speed is constant during the friction phase (see Figure 7).

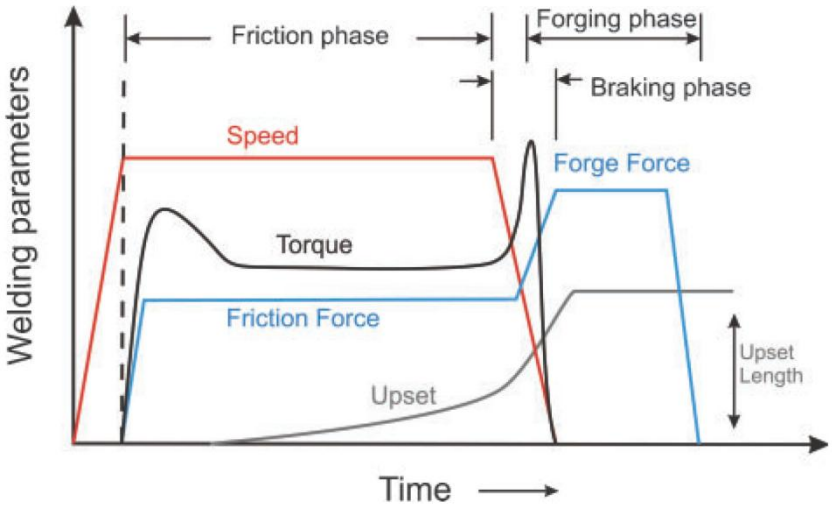

Figure 7: Process parameters for direct-drive friction welding [3]

3.1.2 Friction theory and frictional behavior

To gain a better understanding of the influencing factors and to support the parameter estimation in the experimental part, different views on friction theory and frictional behavior will be discussed according to a literature review of [3].

Generally friction is caused by relative motion (and the related interaction of asperities) of two materials. By conversion of kinetic- into thermal or mechanical energy a temperature increase in the contact area takes place. Due to the fact that a greater amount of force is necessary to start sliding a material than preserve it in motion the static friction coefficient is greater than the dynamic one. Different friction theories exist, such as Amonton's law (introduced in 1699), which states that the friction force is proportional to the load (friction force = coefficient of friction x normal load). Although this law is frequently obeyed it inherits a lack of universality, which is supported by the fact that the friction coefficient decreases with load for different material combinations such as steel on ice or steel on Teflon. Amonton states that the coefficient of friction is a constant and the friction force is only a result of the applied pressure. Furthermore, Coulomb indicated that the friction force is independent of the contact area and the sliding velocity. However, e.g. [10]

demonstrated that the friction coefficient varies with the sliding velocity under different degrees of normal pressure, as shown in Figure 8.

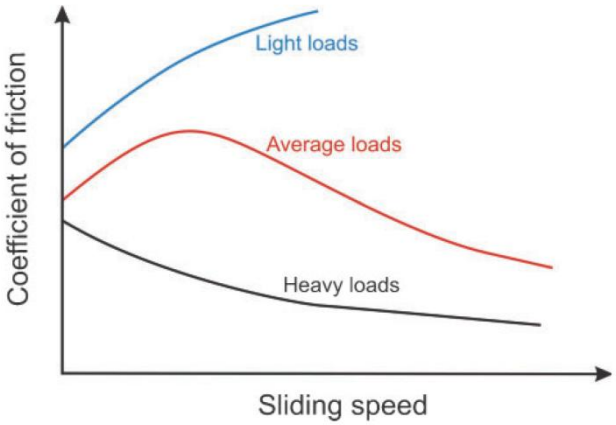

Figure 8: Effect of sliding speed on friction coefficient under different degrees of normal pressure [3]

Moreover, [11] indicated that the coefficient of friction decreases with rotational speed. Additionally, [12] found out that an increased pressure and velocity lead to a decrease of the friction coefficient and that the friction coefficient behavior also depends on the temperature, as shown in Figure 9.

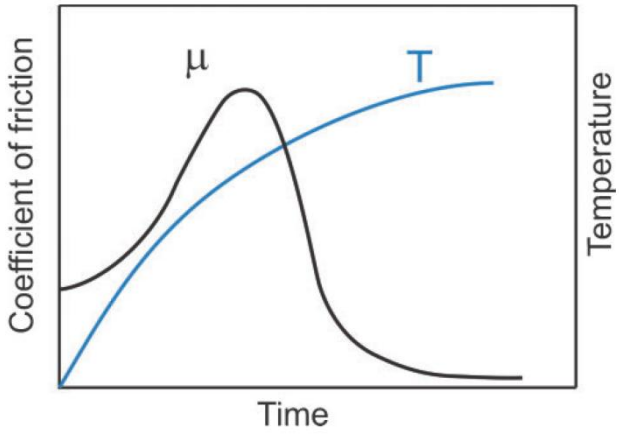

Figure 9: Changes in temperature and coefficient of friction during friction welding of steel [3]

To sum up, five influencing factors according to [13] can be mentioned for friction welding:

1. relative speed
2. the temperature of the friction surfaces
3. the nature of the material
4. the presence of surface films, and
5. the normal pressure.

Due to the fact that the friction coefficient varies during the different friction welding phases, [13] proposed three stages for the heating period: The first stage is characterized by moderate temperature and a low friction coefficient (μ~0.1). The maximum value is related to static friction (μ~0.25) and is represented in the friction torque (Figure 5 and Figure 7). While the asperity contact area increases in the second stage, the third stage is characterized by high temperatures and steady state conditions resulting in plasticized material.

This short insertion shows that it is rather impossible to find the exact coefficient of friction for friction welding. The friction coefficient varies over a wide range and in the best case numerical analyses can reproduce the experimental values. Therefore the optimization of friction welding parameters is still dependent on the trial-and-error method. [3]

3.1.3 HAZ structure

As a basis for the metallographic investigation a characteristic HAZ structure of friction welded (steel-) specimens will be discussed briefly in this subchapter.

According to [3] the HAZ can be divided into four different zones (see Figure 10):

(i) *Contact zone*

In this zone rubbing and material transfer between the two interfaces occurs. The very fine-grained microstructure in this zone is a result of the severe plastic deformation and full recrystallization.

(ii) *Fully plasticized zone*

No rubbing and metal transfer takes place in this zone. However, a considerable amount of plastic deformation occurs. Further, extremely increased dislocation density and dynamic recrystallization due to the high temperatures were documented. The grains are fine and equiaxed.

(iii) *Partly deformed zone*

The strain rate, temperature and plastic deformation is lower than in zone (ii). Hence the microstructure becomes coarser.

(iv) *Undeformed zone*

No plastic deformation takes place. Grain growth may occur in this zone.

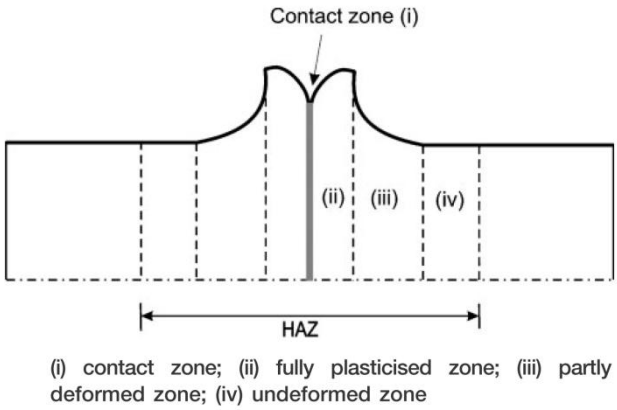

Figure 10: Schematic illustration of different HAZ regions for friction welded specimens [3]

3.2 Material

This chapter shall provide a basic understanding of the material to be welded. The properties of molybdenum and its alloy TZM which is used for the specimens will be discussed. Further, typical applications will be presented.

3.2.1 Properties of Molybdenum

The name molybdenum comes from the Greek word "*mólybdos"* which means "heavy" or "lead" [14]. Molybdenum is a naturally occurring element with a body-centered cubic crystal structure (bcc) and a melting point of 2617 °C (2890 K). It is classified as a refractory metal together with Niobium, Tantalum, Tungsten and Rhenium.

Common characteristics of refractory metals are their high density, high melting points and superior resistance to wear and acid corrosion. Molybdenum (wrought and stress relieved) has with 335 GPa a relatively high Young-modulus and exhibits ultimate tensile strengths' at RT between 450 to 795 MPa. The thermal conductivity of 147 W/(mK) is roughly 50% higher than that of ordinary metals like steel or nickel alloys. Another advantage is that the coefficient of thermal expansion with ~5 µstrain/K is relatively low, compared to other metals, and almost linear with increasing temperature over a wide range (up to ~1100 °C). [12, 13]

Molybdenum and its alloys are produced via powder metallurgy, electron beam or vacuum arc melting, whereby powder metallurgy has several advantages compared to the molten-route methods. One major advantage is the fine-grained microstructure which improves the mechanical properties of the material and also enhances the mechanical processing. [17]

3.2.2 Properties of TZM (Titanium-Zirconium-Molybdenum)

The molybdenum alloy TZM (Titanium-Zirconium-Molybdenum) has a chemical composition as shown in Table 1.

Table 1: Chemical composition of TZM alloy

Titanium – **Z**irconium – **M**olybdenum (**TZM**) dispersion strengthened alloy		in weight %
Chemical composition	Mo Ti Zr C	balance 0.5 0.08 0.01-0.04

The ultimate tensile strength of TZM is in the range of 765 to 1070 MPa at RT. The hardness is 259 HV after EN ISO 6507-1. The density is with 10.10 g/cm³ about 25% higher than that of steel (see Annex: Inspection Certificate). TZM has a higher recrystallization temperature (1400 °C) than pure molybdenum (1100 °C) and a better creep resistance [3, 13].

The superior mechanical properties of TZM are caused by precipitation and dispersion of carbides and oxide particles in the molybdenum matrix [18]. According to Plansee the recommended temperatures of use are between 700 and 1400 °C.

Table 2 gives an overview of the properties of TZM compared to pure molybdenum.

Table 2: Properties of TZM compared to pure molybdenum, ~ comparable with pure Mo, + higher than pure Mo, ++ much higher than pure Mo, - lower than pure Mo [14]

Property	Mo	TZM
Alloy components (percentage by weight)	99.97 % Mo	0.5 % Ti / 0.08 % Zr 0.01 - 0.04 % C
Thermal conductivity	~	-
Stability at room temperature	~	+
Stability at high temperature	~	++ (< 1 400 °C)
Creep resistance	n.s.	+ (>1 400 °C)
Recrystallization temperature	~	+
Ductility after HT use	~	+
Weldability	~	+

3.2.2.1 Ductile-brittle transition temperature

The ductile-brittle transition temperature (DBTT) limits the application of pure molybdenum. Above a certain temperature, depending on several factors such as chemical composition, the level of cold working, internal stress state (see Figure 11) etc., molybdenum loses its brittleness. Other factors such as adding alloying elements like rhenium can lower DBTT even below room temperature (see Figure 12) [14]. “Generally metals with body-centered cubic structure have a very good ductility and toughness at a homologous temperature of (T/T_m (K)) ≥ 0.3, but brittle behavior is observed at a homologous temperature of 0.1 which is near room temperature for molybdenum” ([19], p. 1). According to [20] TZM exhibits the highest low temperature toughness among all Mo-alloys, though in a fully recrystallized state TZM shows a drastic loss in ductility and the DBTT increases above room temperature.

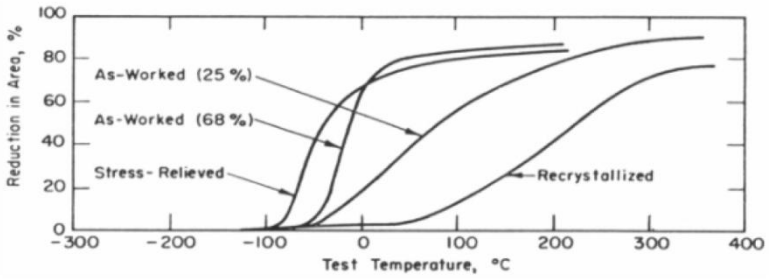

Figure 11: Ductile to brittle transition for different degrees of deformation of Mo [21]

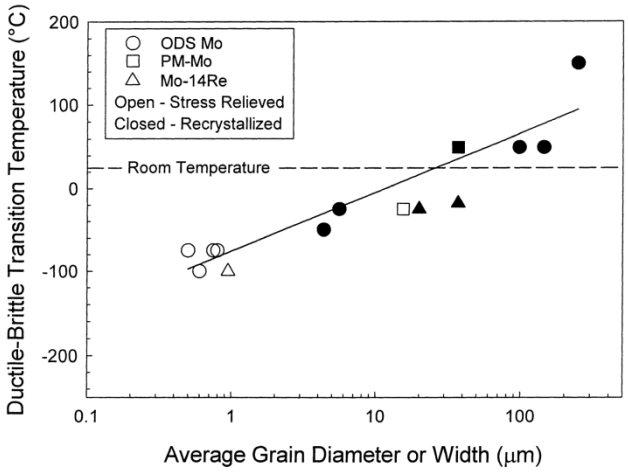

Figure 12: Effect of grain size on the DBTT of unalloyed powder metallurgy molybdenum (PM-Mo) and two oxide dispersion strengthened alloys (ODS Mo, Mo-14 Re) [22]

3.2.2.2 Crack resistance

Although creep resistance and high-temperature strength are the most important attributes for X-ray anodes, fracture resistance plays an important role while loading and unloading the parts from ambient temperatures to operating temperatures. Especially below the ductile brittle transition temperature refractory metals can be seriously affected by brittle cracking.

Mo-alloys exhibit a so-called R-curve behavior which means that the fracture resistance increases during crack propagation. Typical start values for the stress intensities are as low as K_R^0=4-7 MPa√m whereby the fracture resistance quickly increases to K_R values of 30 MPa√m. These values show that crack initiation is more comparable to fully brittle material such as ceramics. However, in contrast to ceramics, Mo-alloy quickly develops a substantial plastic zone which leads to the high K_R plateau values. Furthermore, crack stability increases significantly with increasing temperature, which can be seen in the much steeper initial slopes for elevated temperature R-curves. [23]

Figure 13 shows stress intensity vs crack advancement of two fully recrystallized compact tension (CT) specimens of TZM and MHC alloy.

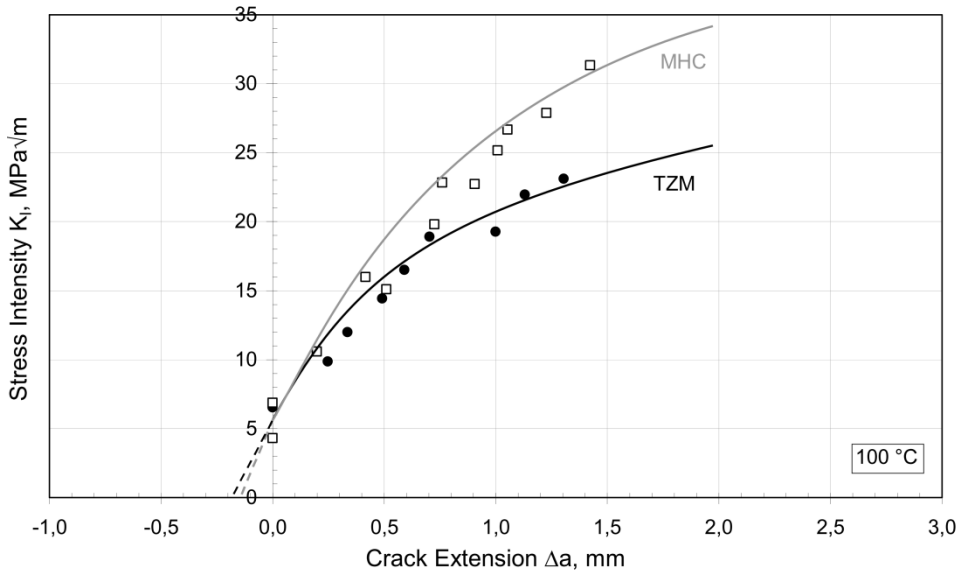

Figure 13: R-curve (crack extension resistance curve) of TZM and MHC at elevated temperature (100 °C) [23]

3.2.2.3 Creep

By quantifying relevant microstructure parameters like grain size, grain disorientation and local texture formation [24] correlated creep test results with the evolution of the microstructure of Mo and TZM. A main finding by comparing the results after a creep test (1400°C, 80h) of pure Mo to TZM was that the grain growth of TZM alloy is impeded by particles, which leads to a delayed recrystallization. Moreover the stress to activate creep deformation is much higher for alloyed Mo. Also investigations of [25] show that adding particles to molybdenum has a beneficial effect on creep rupture behavior and the minimum creep rate at moderate temperatures (<1500°C). Above these temperatures the alloys lose their creep resistance.

Figure 14 shows a stress-rupture plot for Mo, TZM and MHC alloys.

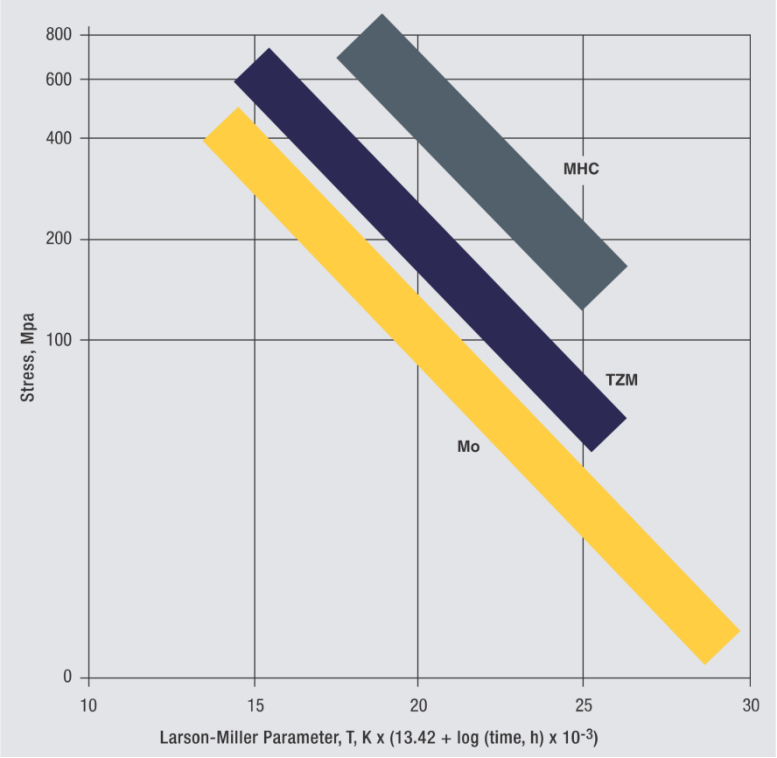

Figure 14: Stress-rupture plot for Mo, TZM and MHC alloys [1]

However, rupture time is not the only decisive factor for creep performance. Another measure is the steady-state creep rate as shown in Figure 15. It can be seen that TZM is far more resistant to deformation than e.g. Mo. Furthermore [24] states that the creep curve of TZM (1400 °C, 80 h) is characterized by a shortened primary creep region and a distinctive minimum creep rate.

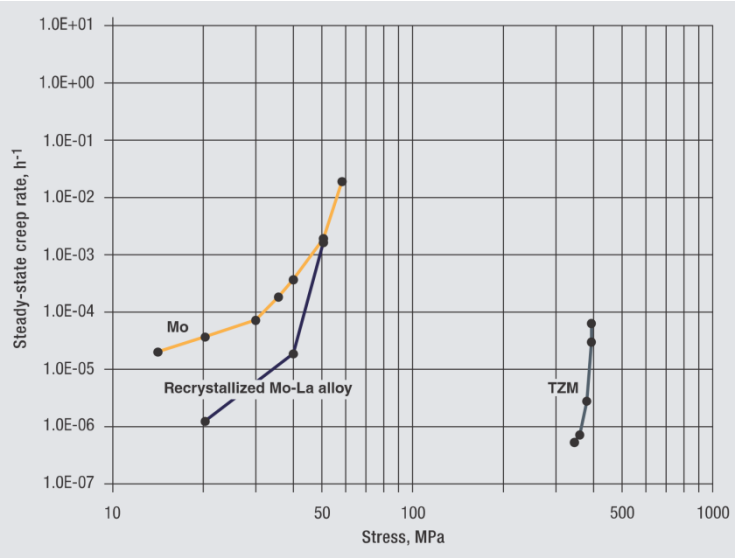

Figure 15: Steady-state creep rate of pure Mo, TZM and MO-La at 1100°C, [6, 7]

3.2.2.4 Recrystallization behavior

Compared to pure molybdenum, the carbide-precipitation-hardened alloy TZM has a 300 degree higher temperature for 100% recrystallization of approximately 1400 °C (annealing duration = 1 hour and degree of deformation = 90%). The recrystallization temperature increases also with an increased degree of deformation. This can be explained by particle refinement, which means that the elongated particles break up into smaller particles after annealing. As a result of the increased particle number the sub-grain boundaries are pinned more effectively and therefore increase the recrystallization temperature. [26] Figure 16 shows the grain size versus the annealing temperature of molybdenum sheet metal.

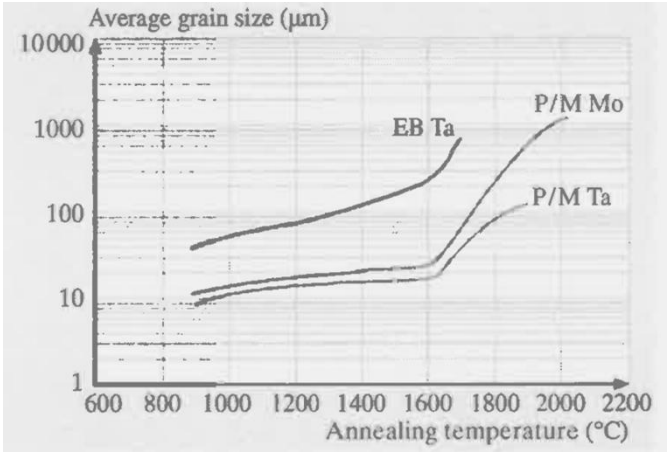

Figure 16: Grain size vs annealing temperature for sheets with a thickness of 1mm (for Mo annealing time =1h and degree of deformation =94%) [26]

3.2.2.5 Influence factors on deformation processes

To support the planning and understanding of the empirical part, this sub-chapter will provide information about influencing factors on the deformation behavior of TZM based on a literature review of [21].

3.2.2.5.1 Flow stress dependency on temperature and degree of deformation

In a microscopic scale, the yield strength is defined as the stress where dislocations are starting to slip, whereas in the macroscopic view it is the stress where the material starts to flow over the whole cross-section. Influencing factors on the deformation of bcc metals are temperature, strain rate, type of stress (compression or tension) and impurities. The model of Seeger describes that the flow stress can be divided into the athermal part and the thermal part. The athermal part only depends on the microstructure (dislocations, foreign atoms, grain boundaries, etc) and occurs over the whole temperature range. There is only a linear influence of the temperature on the shear modulus G, which has to be considered. The thermal part has to be added only below the transition temperature, which was identified for not pre-deformed molybdenum in the range of 340 to 400 K. [21]

Figure 17 shows that the flow stress decreases rapidly at lower temperatures ($T \leq 0.1$ to $0.2\ T_s$) up to the transition temperature T_0 [21]. Further on the increase of work hardening which leads to an increase of the yield strength is represented.

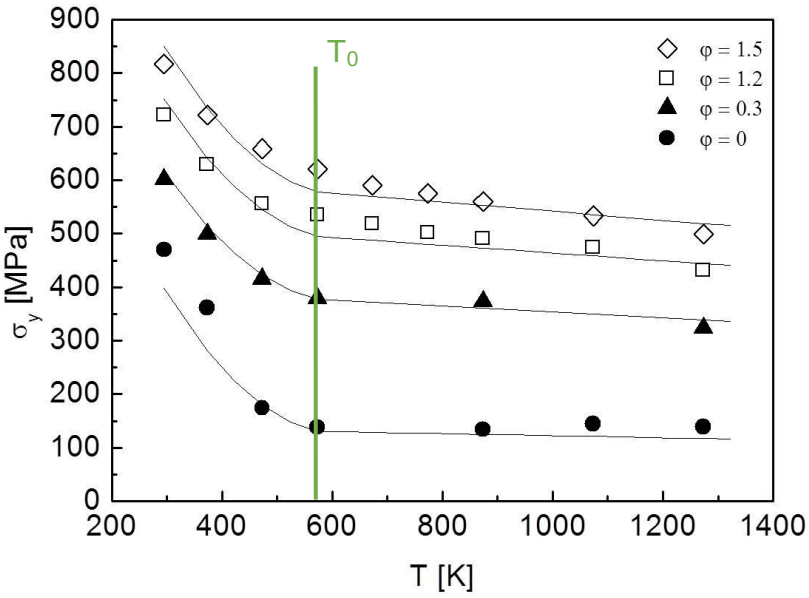

Figure 17: Work hardening of TZM [27]

3.2.2.5.2 Dependency of yield strength on temperature and strain rate

To be aware of the influence of the strain rate which has to be applied in the experimental part, the correlation is shown in Figure 18. At a certain temperature below T_0 an increase of the strain rate leads to an increase of the yield strength. The transition temperature from the thermal to the athermal part also increases with a higher strain rate.

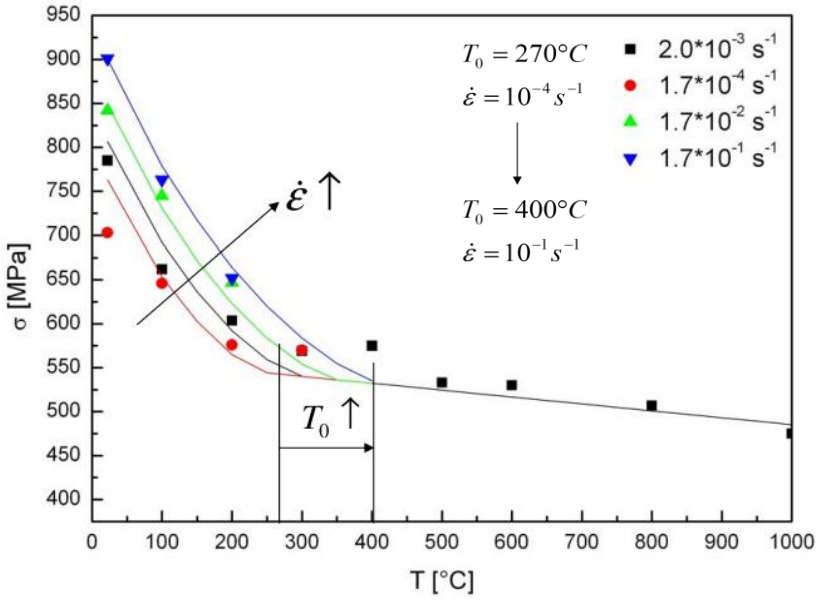

Figure 18: Dependency of yield strength on temperature and strain rate of TZM, predeformation φ=0.8, 55% [28]

3.2.2.5.3 Evolution of hardness over temperature

Figure 19 shows the development of the macro hardness values for TZM depending on the temperature. Starting at an initial value of approximately 260 HV10 at room temperature the hardness decreases sharply to 160 HV10 at 400 °C. Afterwards a slower decrease to 110 HV10 at 1000 °C is documented.

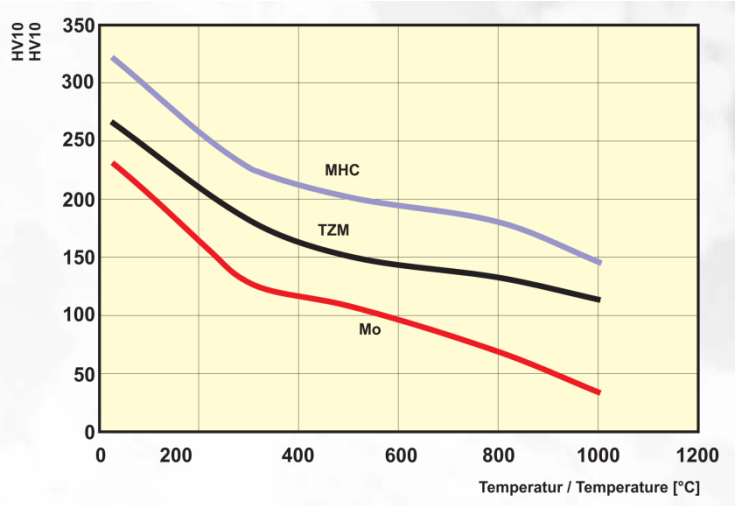

Figure 19: Hardness values for Mo-, TZM- and MHC-rod material (Ø 25mm; stress-relieved condition) depending on temperature [17]

3.2.2.6 Microstructure of TZM

According to [29] zirconium and oxygen form Z_rO_2 precipitations which can be up to 10 µm in size, as shown in Figure 20. The carbon forms molybdenum-carbide (Mo_2C) and molybdenum-titanium-carbides $(Mo,Ti)_xC_y$ (<1µm), whereas at least 0.4 wt. % titanium remains in the molybdenum matrix.

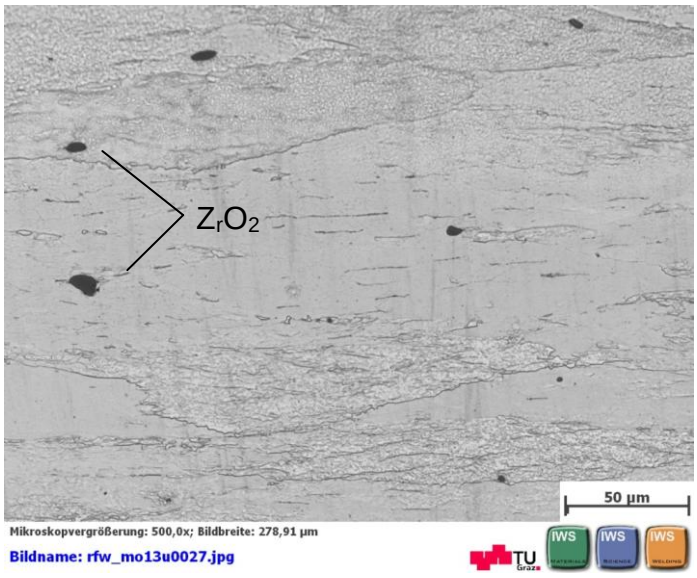

Figure 20: Optical micrograph of TZM, Trans-sectional view on Ø 70mm rod

Investigations in [29] with SEM and TEM show Mo_2C precipitates at the grain boundaries in µm-scale (see Figure 21). Further, it is stated that the main effect of the particles in the Mo-matrix is the increase of the recrystallization temperature by hindering sub-grain movement [29].

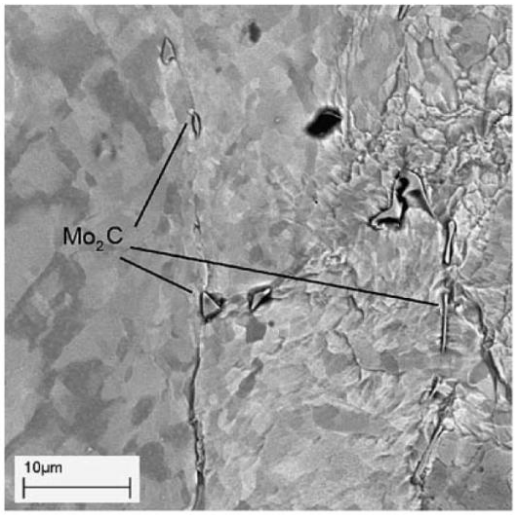

Figure 21: Mo_2C at grain boundaries, SEM [29]

3.2.3 Manufacturing of semi-finished products

Molybdenum is mostly extracted out of molybdenite (MoS_2), which is a by-product of copper production and wulfenite ($PbMoO_4$). The ores contain approximately 0.5% MoS_2 and have to be separated by a flotation process and following roasting to obtain molybdenum-trioxide (MoO_3) which serves (together with ammonium molybdate) as raw material for the production of molybdenum. As shown in Figure 22, these raw materials have to be processed in a two-stage hydrogen reduction process to obtain a fine-grained metal powder of high purity (≥ 99.97%). After adding the desired alloying elements, sieving, mixing and homogenization, molybdenum is pressed into rods or plates either with hydraulic presses (uni-axial) or iso-static presses. Afterwards sintering between 1800 to 2200 °C is conducted. This sintering process increases the mechanical strength and the density of the material. After hot-working (extrusion, forging or rolling) between 1200 and 1500 °C the semi-finished products have to be annealed to obtain the desired microstructure [17].

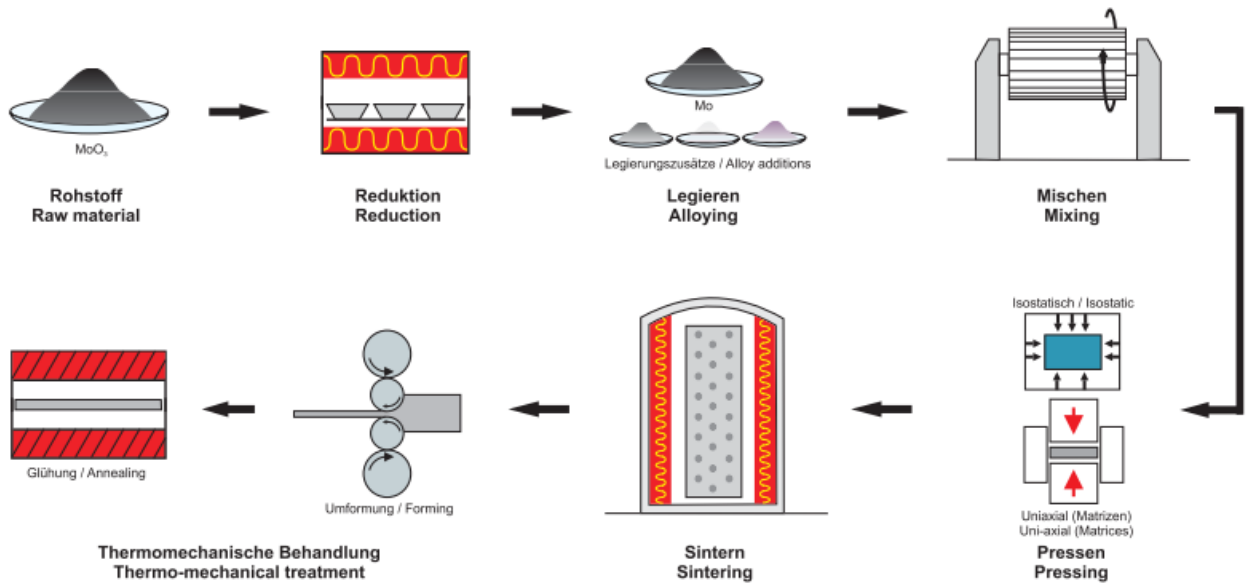

Figure 22: Schematic flow of the production of semi-finished products [17]

3.2.4 Applications of molybdenum and its alloy TZM

Related to its properties such as high strength and stability at high temperatures, molybdenum and its alloys have a wide range of use. Its resistance against molten metals and the good thermal shock resistance are reasons for using it in hot-forming tools. TZM for example is used to forge nickel-base super alloy components at temperatures of about 1200 °C. Another field of usage is the lighting and electronic industry due to molybdenum's strong bonding with glass. [1]

This work is related to the medical industry where rotating TZM anodes are used in X-ray tubes as shown in Figure 23 and Figure 24. Dynamic loads, high rotational speed (~ 10,000 rpm) and high temperatures (max. 1500 °C) are typical for this application.

Figure 23: X-ray target showing rotor (A), stem (B) and TZM alloy target (C) with integral tungsten-rhenium alloy track (D) for x-ray generation, furthermore the graphite heat sink (E) and cathode cup (F) that contains the tungsten filament [1]

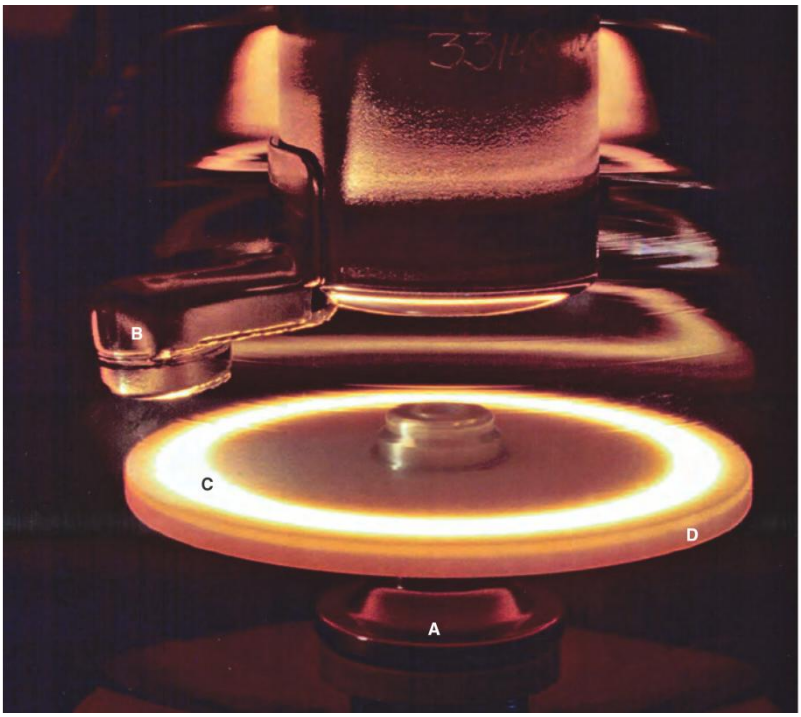

Figure 24: The TZM target (D) rotates with high speed, driven by the TZM rotor (A). The tungsten filament is heated to high temperatures within the cathode cup (B) and emits electrons that are focused on the W-Re focal tack (C). [1]

4 Experimental

This chapter includes information about the used welding machine, the material, the specimen geometry, the welding parameters as well as the description of the welding procedure including the PWHT.

The welding tests have been executed at Klaus Raiser GmbH in Eberdingen, Germany, on the 15th of January 2014.

4.1 Welding parameters

A main objective of this thesis was to ensure reproducibility of the already reliable inertia-drive friction welding bonds on the available direct-drive machine.

Therefore the start parameters for the experiments were found through a rough estimation on the basis of the energy input into the welding interface. To obtain a proper weld, the welding energy and/or power density should be the same for both processes. An averaged constant friction coefficient of 0.14 has been calculated out of the inertia drive process (see Chapter 4.1.2.2). Therefore the results should be considered critically because the coefficient of friction depends on several parameters such as rotational speed, normal pressure, temperature and chemical composition. Due to these influencing factors which are not constant (e.g.: heat generation in the interface), the friction-coefficient also varies during the different phases of the friction welding process, as discussed in the literature review [3]. Another factor to consider is that the thermal conductivity of molybdenum is with 147 W/(mK) (at RT) approximately three times higher than that of unalloyed steel. Therefore a short friction time, like it is applied in the inertia-drive process, is crucial to get the necessary heat accumulation in the welding area.

4.1.1 Frictional heat generation model

Based on the assumption of a uniform heat generation and pressure across the interface, the following model related to [30] was used to estimate the scale of welding parameters. The influence of the heat transfer as well as the plastic deformation was neglected. Figure 25 visualizes the friction surface and relevant variables.

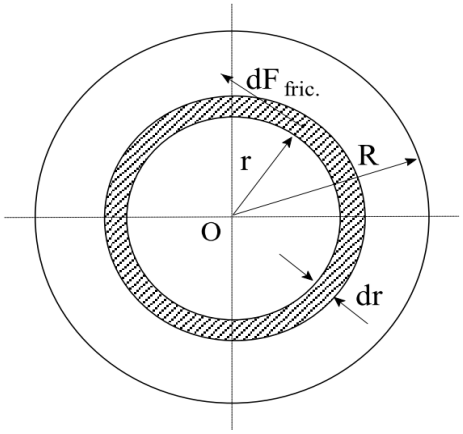

Figure 25: Friction surface sketch [9]

The constant pressure p acting on the surface dA equals the differential force dF.

$$dF = p\,dA = 2p\pi r\,dr$$

Since dF is equivalent to the equal and opposite normal acting on dA, the differential frictional force dF_f, can be specified as

$$dF_f = \mu\,dF = 2\mu p\pi r\,dr$$

with μ being the friction coefficient. It is known that the tangential velocity v_r is the same at any point of one radius r:

$$v_r = r\omega = r2\pi n$$

with ω being the angular velocity and n equalling the rotational speed.

The differential power to rotate the area dA is

$$dP = dF_f(v_r) = 2\mu p\pi r^2\omega\,dr$$

Therefore, by integrating this equation with respect to r, the frictional heating power is obtained as

$$P = \int_{R_{inside}}^{R_{outside}} 2\mu p\pi r^2 \omega \, dr = \frac{2}{3}\mu p\pi r^3 \omega = \frac{2}{3}\mu p\pi (R_{outside}^3 - R_{inside}^3)\omega$$

The welding energy E is obtained by multiplying the power P with the friction time t_f.

$$E = Pt_f$$

The power density ψ which refers the power P to the intersection area dA equals to

$$\psi = \frac{P}{A}$$

4.1.2 Parameter estimation

This chapter presents the results of the parameter estimation according to the model described in the previous chapter.

4.1.2.1 Estimation of power density based on inertia drive parameters

As mentioned above, the power density should serve as a basis for estimating the direct-drive friction welding parameters. Therefore the input values of the existing inertia drive process as shown in Table 3 were used for the calculation shown in Table 4.

Table 3: Inertia drive input values for power density calculation

Input	Symbol	Physical quantity
Welding energy	E	252000 J
Friction time	$t_{f\_inertia}$	3 s
Weld contact area	$A_{f\_inertia}$	1570 mm²

Table 4: Power density calculation for inertia drive process

Output	Calculation	Result
Power	$P_{inertia} = \frac{E}{t_{f\_inertia}}$	84 kW
Power density	$\psi_{inertia} = \frac{P_{inertia}}{A_{f\_inertia}}$	53 W/mm²
Specific welding energy	$E_{spec.\_inetria} = \frac{E}{A_{f\_inertia}}$	161 J/mm²

4.1.2.2 Estimation of averaged μ based on inertia-drive parameters

Table 5 and Table 6 show the input values as well as the calculation for the reconstruction of the averaged friction coefficient out of the inertia-drive process.

Table 5: Input values for the estimation of an averaged friction coefficient

Input	Symbol	Physical quantity
Power	$P_{inertia}$	84 kW
Friction force	$F_{f\_inertia}$	60 kN
Initial rotational speed	$n_{o\_inertia}$	3800 rpm
Outside radius	$R_{outside}$	60 mm
Inside radius	R_{inside}	40 mm
Weld contact area	$A_{f\_inertia}$	1570 mm²

Table 6: Friction coefficient calculation for inertia-drive process

Output	Calculation	Result
Friction pressure	$p_{f\_inertia} = \frac{F_{f\_inertia}}{A_{f\_inertia}}$	38 MPa
Angular velocity	$\omega = 2\pi n_{0\_inertia}$	398 s^{-1}
Average friction coefficient	$P_{inertia} = \frac{2}{3}\mu p\pi(R_{outside}^3 - R_{inside}^3)\omega$	
	$\mu = \frac{3P_{inertia}}{2p_{f\_inertia}\pi(R_{outside}^3 - R_{inside}^3)\omega}$	~ 0.14

4.1.2.3 Estimation of nominal and actual direct-drive parameters

Table 7 shows the input values for the estimation of the direct-drive parameters. This calculation (see Table 8) shows the nominal parameters to achieve a power density of 53 W/mm² and additionally the results for the actual parameters applied in the experimental part. Due to limited machine capacity, the actually applied parameters differ from the originally intended estimated nominal values.

Table 7: Input values for the estimation of the direct-drive parameters (nominal values) as well as for the reconstruction of the actually applied parameters

Input	Symbol	Nominal value	Actual value
Friction force	F_{f_direct}	113* kN	70 kN
Rotational speed	n_{direct}	1500** rpm	1500 rpm
Friction time	t_f	3 s	3 s
Outside radius	$R_{outside}$	55 mm	55 mm
Inside radius	R_{inside}	40 mm	40 mm
Weld contact area	A_{f_direct}	1120 mm²	1120 mm²

* Iterated variable to obtain a power density of 53 W/mm²

** maximum rpm-limit of the available machine

Table 8: Calculation of the command variables as well as reconstruction of the actually applied parameters

Output	Calculation	Results (nominal values)	Result for applied parameters
Angular velocity	$\omega = 2\pi n_{direct}$	157 s^{-1}	157 s^{-1}
Average friction coefficient	assumed from inertia-drive process	~ 0.14	n.s.
Friction pressure	$p_{f\_direct} = \frac{F_{f\_direct}}{A_{f\_direct}}$	100 MPa	63 MPa
Power	$P_{direct} = \frac{2}{3}\mu p\pi(R_{outside}^3 - R_{inside}^3)\omega$	60 kW	37 kW
Power density	$\psi_{direct} = \frac{P_{direct}}{A_{f\_direct}}$	53 W/mm²	33 W/mm²
Specific welding energy	$E_{spec.\_direct} = \frac{P_{direct}\, t_f}{A_{f\_direct}}$	161 J/mm²	98 J/mm²

4.1.3 Applied parameters

Together with the highest possible spindle velocity of 1500 rpm a friction pressure of approximately 63 MPa was applied for 3 seconds. Afterwards a forge pressure of 268 MPa was held for 10 seconds. These parameters result in a total specific energy input of about 98 J/mm² and a power density of 33 W/mm². Figure 26 shows a schematic diagram of the applied parameters.

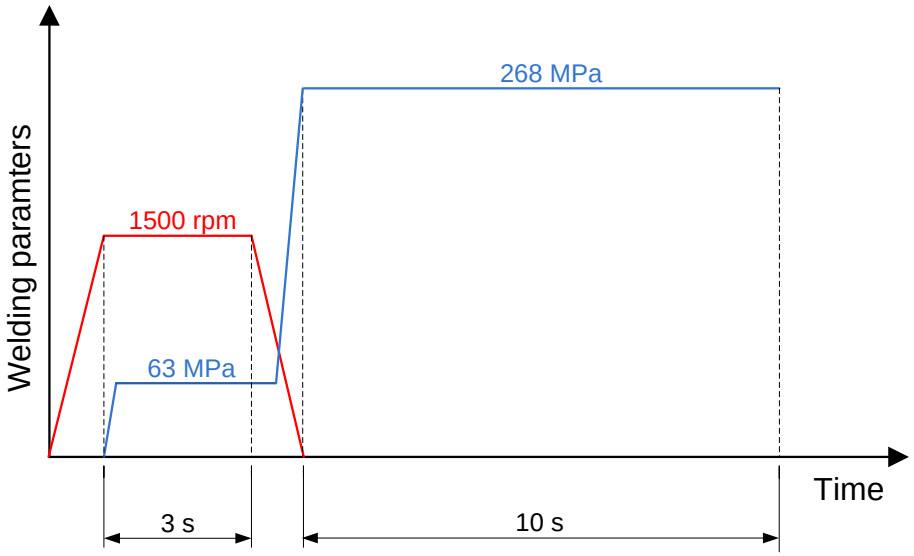

Figure 26: Schematic visualization of the applied welding parameters

4.2 Discussion of applied parameters

However, before accomplishing the first proper welding results with the parameter set described in the previous chapter, several iterative steps – which resulted in defective weld specimens (see Chapter 6.9) – were necessary to find the appropriate machine settings.

Table 9 shows the parameters used for inertia-drive welding compared to the direct-drive ones applied in the experiments. As already discussed above, the objective was to achieve a nominal power density of 53 W/mm² for this welding process. However, it has to be remarked that there is still scope for optimization supposed. However, the available machine capacity limited the friction pressure to 63 MPa and 1500 rpm which resulted in a reduced maximum power density of 33 W/mm². In combination with the test results, this energy input into the welding interface can be considered as insufficient for this application, although the previously considered crucial quality

criteria of the axial shortening has been achieved. However, it is possible that the material was not hot enough and that the upset was only reached by the very high forge force of 268 MPa (~ four times the friction force). The inertia drive process for TZM already shows good weld properties by applying a forge force approximately twice as high as the friction force.

Table 9: Comparison of inertia-drive (provided by Plansee) to direct-drive friction welding parameters

Parameter	Unit	Inertia drive	Direct drive	
			Calculated (nominal values)	applied
Weld contact area	mm^2	1570	1120	1120
Preheat temperature	°C	500	-	390
Rotational speed	min^{-1}	3800	1500	1500
Welding energy	kJ	252	179	110
Specific welding energy	J/mm^2	161	161	98
Power density	W/mm^2	53	53	33
Welding / friction pressure	MPa	38.2	100	62.5
Forge pressure	MPa	95.5	200	268.1
Welding / friction time	sec	3	3	3
Dwell / forge time	sec	25	10	10
Axial upset	mm	4-5	≥ 4.5	6.6

4.3 Welding machine

The welding was carried out by Klaus Raiser GmbH using a Toyoda FW60TC direct-drive machine with 18 kW electrical motor power. The maximum spindle speed equals to 1500 rpm, and the axial force capability of the weld facility is limited with 300 kN.

A shortcoming of this machine is that it is not possible to record the actual values during the weld process. Therefore only the input (nominal) parameters were documented.

Figure 27: Toyoda friction welding machine

4.4 Material

The raw material is a uniform batch of almost 50 kg TZM produced via PM route as described in Chapter 3.2.3. Starting with an initial diameter d_0=140 mm, five forging steps lead to a final diameter of the raw material of d_1=70 mm. The degree of deformation for this forged TZM rod is specified as

$$degree\ of\ deformation\ [\%] = \frac{d_0^2 - d_1^2}{d_0^2}$$

$$degree\ of\ deformation\ \varphi\ [-] = ln\frac{d_0^2}{d_1^2}$$

which equals to 75% (φ=1.4).

Heat treatment (stress-relief annealing) at 1100 °C for 2 hours has been executed after forging.

Representative batch properties of semi-finished TZM are summarized and referenced to ASTM in Table 10.

Table 10: Material parameter of TZM batch used for direct-drive friction welding experiments

Titanium – **Z**irconium – **M**olybdenum TZM: dispersion strengthened alloy		Specified acc. ASTM B387 - 10	Batch 239897
Chemical composition in µg/g	Mo	balance	balance
	Ti	4000 - 5500	4423
	Zr	600 - 1200	708
	O	< 500	225
	C	100 - 400	364
Tensile Strength	MPa, RT	>620	765
Yield Strength	MPa, RT	>550	771
Fracture elongation	%	>10	32
Hardness	HV10	240 - 290	259
Density	g/cm³	>10,10	10,18

4.5 Specimens

The raw material described in the previous chapter was further processed to 20 semi-finished rods with 70 mm outside diameter and 55 mm in length. Afterwards it was turned to the originally intended specimen geometry of OD 60 mm and ID 40 mm.

However, a previous estimation of the necessary engine capacity showed that the available machine is not sufficient for these originally intended specimens with an outer diameter of 60 millimeters. Despite this concern, Raiser GmbH was still confident to achieve a proper weld, arguing that steel parts of the same dimensions had been welded successfully on this machine. Nevertheless, at the end the engine was overloaded with the TZM parts. Measures like a flatter acceleration ramp and the reduction of the friction force did not lead to noticeable changes.

After several trials on the original specimens the outer diameter was reduced to 55 millimeters, resulting in a reduction of the welding interface of about 30%. (see Figure 28). Finally the new wall thickness of 7.5 mm resulted in a weld contact area of 1120 mm².

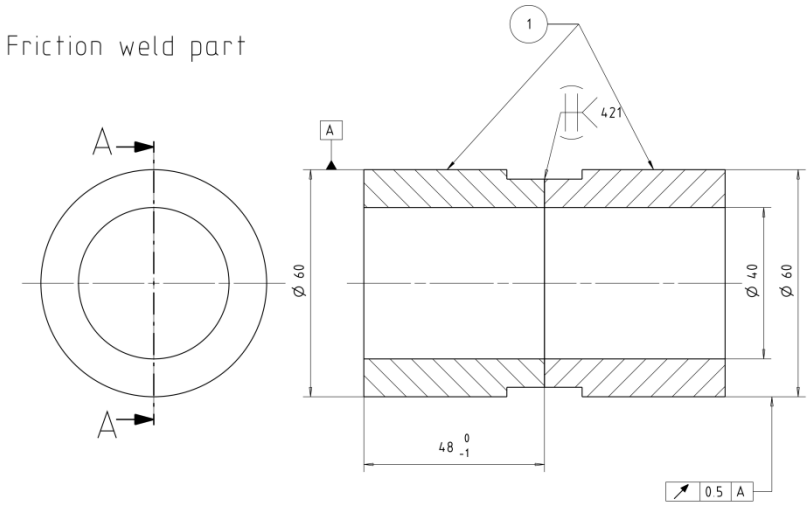

Figure 28: TZM weld specimen, contact area adapted to the available machine capacity

4.6 Welding procedure

In order to support the total energy input, the specimens were preheated in an oven to T~390 °C for about one hour. The surface temperature next to the flash, immediately after welding, was about 430 °C. To achieve slow heat dissipation, the welded parts were cooled in three steps. After cooling in the oven at T~390 °C, the oven was switched off and the door was opened to reach temperatures below 390 °C. The last step was cooling from 150 °C (specimen surface temperature) to room temperature in free convection mode on a fire clay brick.

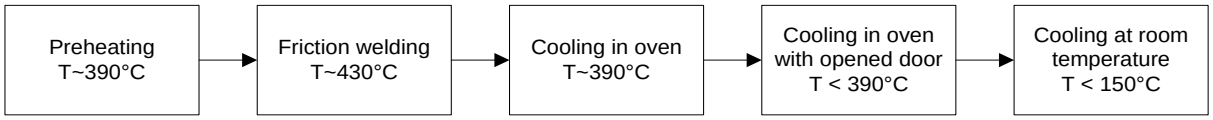

Figure 29: Welding procedure

4.7 Post-weld heat treatment

To relieve residual stresses caused by welding, the standard post-weld heat treatment for this application was applied. Therefore the welded assemblies were annealed in a high vacuum furnace (see Figure 30) at an elevated temperature of 1550 °C for about 1.5 hours dwell time. At this temperature recrystallization took place already. However, due to the fact that the temperatures during the typical application reach the same values, the mechanical properties are still sufficient.

Figure 30: High-vacuum furnace and weld assemblies after PWHT

5 Investigations

Weld qualification was executed according to [31] by means of visual, dimensional, mechanical and non-destructive testing procedures, including ultrasonic and dye penetration testing. Moreover, hardness measurements and light microscopy supported the investigations.

Due to the limited time and specimen resources and owing to the allocation of the investigations to two sites (Graz and Reutte), a test matrix as shown in Table 11 was necessary. Therefore not all tests were applied to one weld specimen. However, comparability is still given in that the identical welding parameters were used for all specimens.

Table 11: Test matrix for successfully welded TZM specimen from January 15th, 2014; ✓ =executed tests, "empty"=not executed tests

Single parts	Welded part	VT	UT	PT	Tensile Test	HT, LiMi, Flash	Location
FWT-09	W-05	✓				✓	Graz
FWT-10							
FWT-11	W-06	✓			✓		Reutte
FWT-12							
FWT-13	W-07	✓	✓	✓			Reutte
FWT-14							
FWT-15	W-08	✓				✓	Graz
FWT-16							
FWT-17	W-09	✓			✓		Reutte
FWT-18							
FWT-19	W-10	✓	✓	✓			Reutte
FWT-20							

5.1 Visual tests (VT)

A visual inspection of weld assemblies was conducted after heat treatment as described in the [32]. Each of the five weld specimens was examined with optical magnification instruments. The inner and the outer flash formation were checked on irregularities and cracks.

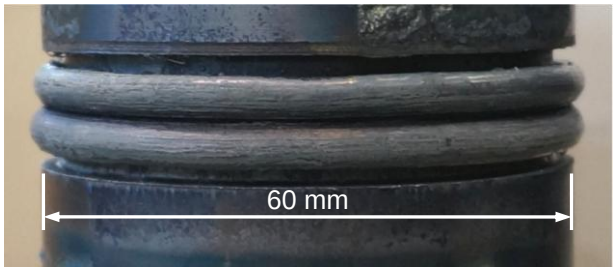

Figure 31: Visual inspection of weld flash prior to heat treatment

5.2 Dimensional check

A dimensional check was carried out on all parts before and after welding. By using calipers, gauges and try squares linear measures, perpendicularity and concentric run-out were documented.

Figure 32: Perpendicularity and concentric run-out documentation

The total length before and after welding was determined with a digital gauge as shown in Figure 33. The difference between these two measures equals the upset reached during the welding process, which is a crucial quality attribute.

Figure 33: Determination of total length before and after welding with a dial gauge

After visual inspection and dimensional check, further machining was necessary for flash removal in order to enable NDE by means of UT and PT.

5.3 Ultrasonic tests (UT)

The ultrasonic test was executed on an immersion-technique test bed (Scan Master LS 500) applying the pulse-echo method according to [33]. Therefore the specimen was fixed on a turntable in deionised water, which serves as a coupler. The stationary transmitter/receiver has a frequency of 10 MHz with a focus at 50.8 mm (2 inches) and focus diameter of 0.8 millimetres. The distance between the transmit/receive head and the specimen entry wall was 45 millimetres. The fact that the focus point is situated 4.2 mm in front of the welding interface is a characteristic of this test method and based on Plansee internal experience. The explanation for this set-up according to [34] is the following: No accurate measurement of the echo is possible within the near (sound) field, due to interferences and the influence of the sending impulse. Therefore the measurement results are gained within the focus zone between the focus point and the far (sound) field. (See Figure 34)

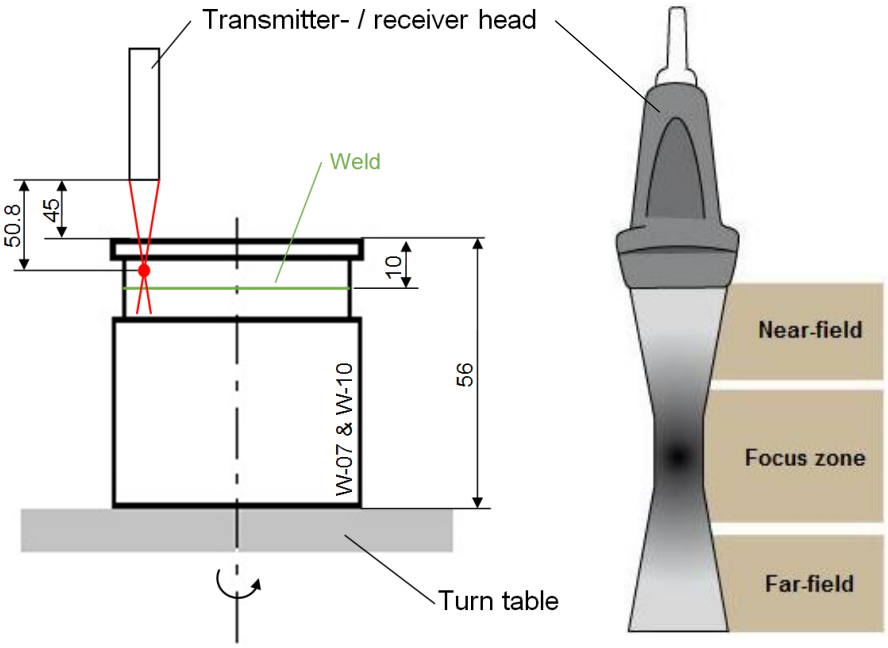

Figure 34: Visualization of test adjustments for UT (all measurements in mm) and schematic illustration of ultrasonic beam fields [35]

5.3.1 Sampling of UT specimen

The welded parts were cut to a total length of about 56 millimeters so that the distance between the front wall and the weld was about 10 millimeters, which was necessary for the measurement setup. After the first test session including the inner and outer flash, machining to the initial dimensions (55 mm OD, 40 mm ID) was executed to visualize potential changes in the boundary areas. (See Figure 35)

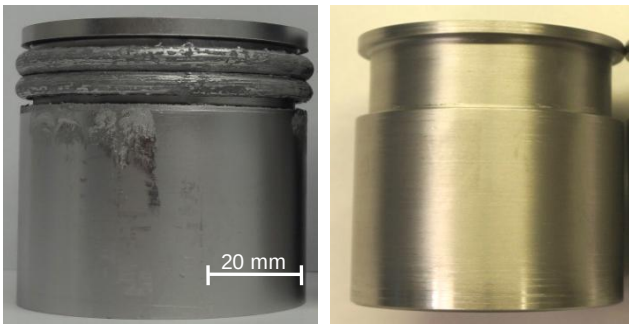

Figure 35: UT specimen W-07 before and after flash removal

5.4 Penetrant tests (PT)

This test was conducted for the samples of the UT test and the tensile test specimens. The test was applied according to [36]ÖNORM EN 571-1 with a fluorescent dye penetrant. Therefore the pre-cleaned specimens were immersed in Magnaflux Zyglo penetrant oil (ZL27A) for 20 minutes. After washing with water the specimen were dipped in a Magnaflux Zyglo emulsifier (ZR10C) for 30 seconds. As a last step the parts were cleaned, dried and powdered with a dry-developer (ZP4B) for further inspection with an UV lamp.

This method allows the detection of cracks greater or equal to 10 µm in depth and 1 µm in width.[1]

5.5 Hardness tests (HT)

The hardness tests were carried out on an automatic hardness measurement machine (Emco-Test, M1C 010) according to [37]. The aim of this test was to get a hardness distribution profile over the whole welding area. Therefore a test force of 98.07 N with a dwell time of 15 seconds was applied to obtain the HV10 hardness values.

For this test the samples from the microstructure specification were used.

5.6 Tensile tests (TT)

The test was performed orthogonal to the welding interface for the weld assemblies W-06 and W-09 and in reference to the raw material at ambient and elevated temperature (1200 °C) according to [38]. The test conditions are shown in Table 12.

[1] Plansee-internal empirical values for testing TZM welds (acc. to Niklas Wex)

Table 12: Test conditions for room and elevated temperature

Test set-up	Unit	Room temperature	Elevated temperature
Test temperature	°C	22	1200
Test machine		Z050 / 50kN	SIMO 86 / 100kN
Displacement sensor		MultiXtense	MT20
Sample design*		RRS	RRB
Measuring length L_0	mm	20	20
Sample diameter d_o	mm	4	4
Pre-load	MPa	20	8
Rate of stress increase (up to the upper yield point)	MPa/s	30	not specified
Test velocity	mm/min	5	2

* see Figure 36 and Annex for Details

For the elevated temperature test the samples were heated in vacuum (to prevent oxidation) for about 45 minutes. After 10 minutes dwell time at 1200°C the tensile test was executed by applying an electro-mechanic pull force. The chromium-nickel thermo element was in direct contact with the test sample, whereas the displacement sensor was fixed on the traverse outside the furnace. Afterwards the furnace was switched off and cooling in free convection for 1.5 hours took place.

In contrast to the elevated temperature test the displacement sensor for the room temperature test was in direct contact with the tensile test specimens, providing more accurate results by avoiding the influence of the intermediate pieces.

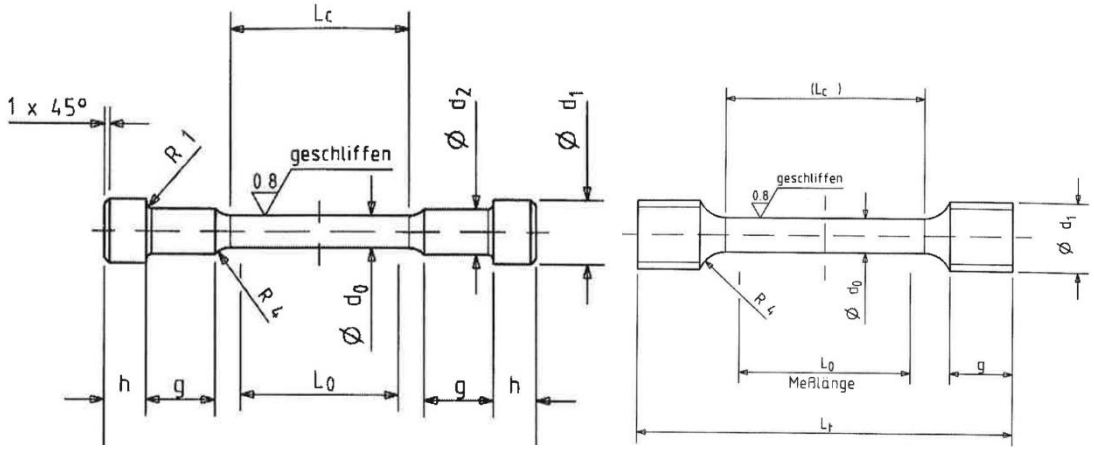

Figure 36: Tensile test samples for room temperature (left) and elevated temperature (right) tests, d_0=4 mm, L_o=20 mm

5.6.1 Sampling of TT specimen

The tensile test specimens were machined out of the weld assemblies by means of wire erosion (see Figure 37). Subsequent turning to d_0=4mm and L_0=20mm was applied to achieve the final dimensions as shown in Figure 36. To maintain comparable results, the sample diameter and the measuring length were chosen the same for the room- and the high-temperature test. Due to the fact that the tensile test samples were machined out of the pipe wall (see Annex), which limited the maximum dimensions, a different design in the clamping area of the sample was necessary. Therefore the Plansee-internal standard samples RRS (shoulder head) and RRB (thread head) were used (see Figure 36). Four high-temperature samples (RRB 4x20) and three room-temperature samples (RRS 4x20), distributed across the circumference, were taken from each of the two weld assemblies, resulting in 14 welded tensile specimens.

Figure 37: Sampling of tensile test specimens from W-06 (same sampling for welded assembly W-09)

The tensile strength at room temperature for the raw material was given in the material-inspection-certificate, whereas three reference samples for the high-temperature test were taken from the left over raw material, as shown in Figure 38. Additionally, tensile test results for the raw material after heat treatment were extracted from the Plansee Material Database.

An overview of the conducted tensile tests and results is shown in the experimental part in Table 17.

Figure 38: Sampling of raw material specimens (RL2-RRB 1. 2, 3) for 1200 °C tensile test

5.7 Metallography

The metallographic investigation was carried out on a Zeiss Observer.Z1m light microscope with a magnification range from 2.5 to 200 times the real size. Furthermore SEM investigations on a Zeiss Leo 1450VP were conducted. The SE and RE micrographs were recorded under vacuum (10^{-4} mbar) and an acceleration voltage of 10 kV. EDX investigations were applied with a Bruker Quantax 400 detector.

The aim of these investigations was to clarify questions concerning the microstructure of the raw material as well as changes of the microstructure caused by the welding process (e.g.: grain growth, texture, etc.).

5.7.1 Microstructure specimen preparation

Figure 39 shows the process steps for the specimen preparation to allow a first microstructural characterization of the material to be welded.

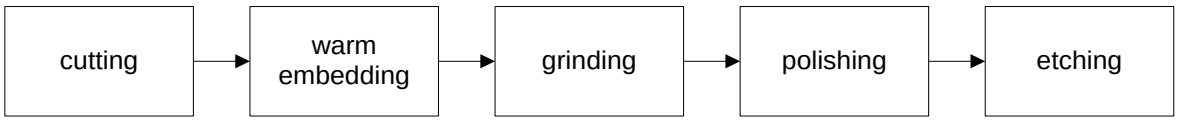

Figure 39: Process steps for specimen preparation

After marking the TZM specimen as shown in Figure 40 and Figure 41, they were cut on a Conrad-Woco-Top350 with the Struers cutting disk 40A30 and cooling liquid. The warm embedding took place on a Struers-CitoPress-20 with DuroFast epoxy hot mounting resin. Afterwards grinding and polishing was accomplished on a Sturers-

Tegra-Force-5 with a granularity as shown in Table 13. The last preparation step was etching with Murakami (100 ml H_2O, 10g K3 [Fe(CN)6], 10g KOH) for 30 seconds [39].

Table 13: Steps for grinding and polishing of the specimen

Step	Grinding	Polishing
1	80	
2	180	
3	320	
4	800	
5	1200	
6	2400	
7	4000	
8		3 µm
9		1 µm

5.7.1.1 Microstructure sampling of TZM rod

The sampling for the microstructure specimen is shown in Figure 40. Specimen 1 was embedded to get a cross-sectional view whereas specimen 2 and 3 were prepared for a trans-sectional view.

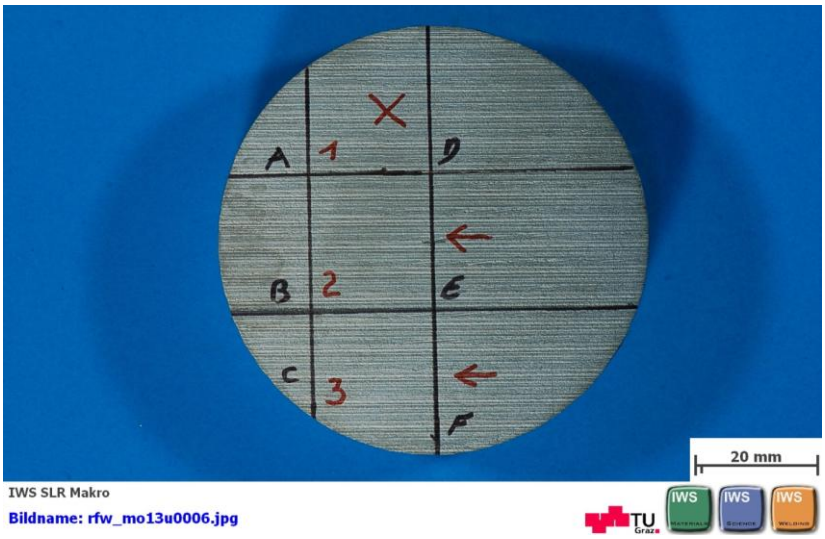

Figure 40: TZM specimen before machining, x = cross-sectional view on embedded specimen 1, ← = trans-sectional view on embedded specimen 2 and 3

5.7.1.2 Microstructure sampling of welded parts

Due to the uncertainty of the width of the heat-affected zone, three microstructure specimens have been cut out of the welded parts W-05 and W-08, as shown in Figure 41.

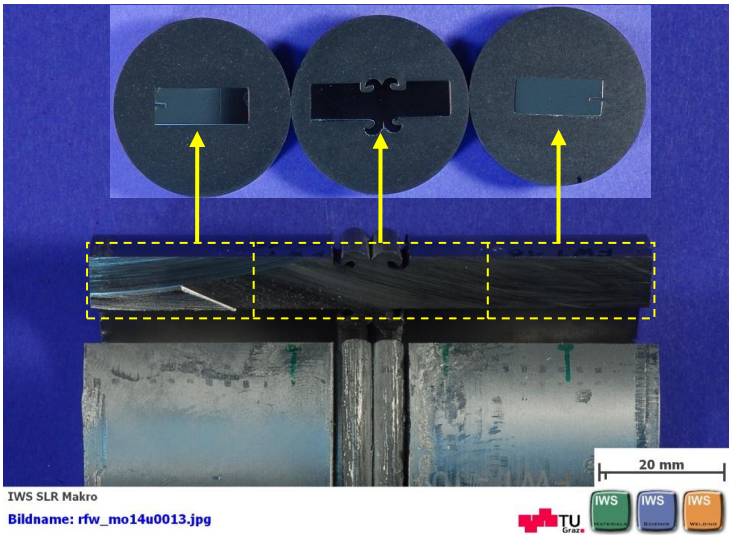

Figure 41: Sampling out of the welded part W-05 (same sampling for welded assembly W-08)

6 Results

This chapter sums up the results gained in the experimental part. The structure of this chapter is related to the previous Chapter (Investigations).

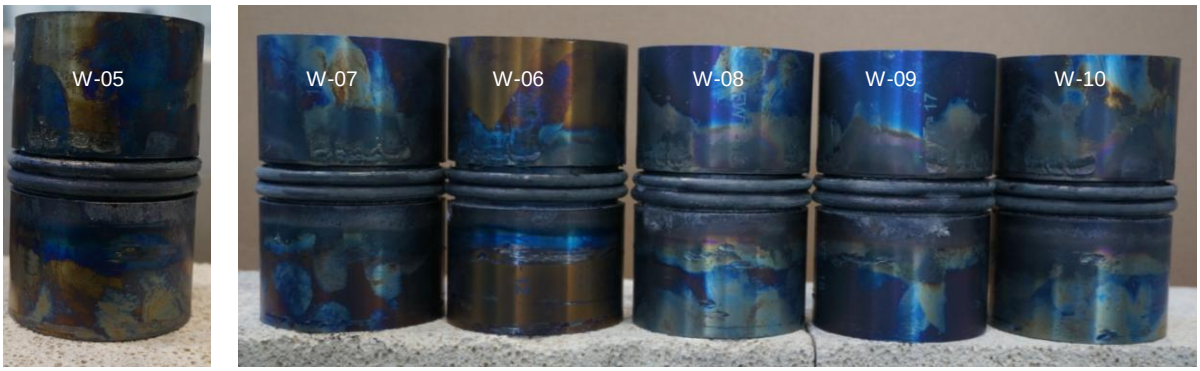

Figure 42: Successfully welded specimens (welding order = left to right)

Figure 42 shows the successfully welded specimens. The nomenclature of the weld assemblies is related to that of the single parts as already visualized in Table 11 (e.g. FWT-09 + FWT-10 result in W-05). Hence, W-07 was welded before W-06 caused by a mistake of the machine operator.

6.1 Visual test results (VT)

All specimens which passed the visual inspection (W-05…W-10) were released for further investigations. The other parts (W-01…W-04) were used for machine calibration and parameter determination and are further discussed in Chapter 6.9.– Defective Specimens.

Table 14: Visual test on irregularities and cracks of the outer and inner flash, OK=VT passed, NOK=VT not passed

Part ID	W-01…W-04	W-05	W-06	W-07	W-08	W-09	W-10
Outer flash	NOK	OK	OK	OK	OK	OK	OK
Inner flash	NOK	OK	OK	OK	OK	OK	OK

6.2 Dimensional check (upset determination)

As known from proper welds of the inertia-drive process, the total upset after welding should be greater than or equal to 4.5 millimeters. All of the parts reached this limit. Besides one exception (W-06), the average upset was about 6.8 millimeters (see Table 15).

As shown in Figure 42, part W-06, which has not reached the average upset of the other five samples (although the machine parameters were the same), has a different annealing color. Furthermore, the measured surface temperature after welding was 50 degrees lower than that of the other specimens. The temperature difference before welding (approximately 20 degrees) due to an unintended shorter exposure time in the oven could be the reason for the lower upset.

Table 15: Total upset after welding, nominal value ≥ 4.5 mm

Assembly ID	Upset after welding
W-05	6.9
W-06	5.5
W-07	6.8
W-08	6.8
W-09	6.9
W-10	6.8

6.3 Ultrasonic test results (UT)

The gate height was chosen with 50%, which means that sound intensities below 50% are not displayed in the error-image. As shown in Figure 43 and Figure 44, the green area represents a defect-free weld, whereas blue areas indicate a defect. Single minor defects can be seen near the inner and outer radius of the weld specimens. Most of the welded cross section shows no defects. The continuous blue line at the outer circumference is an unintended boundary effect (of the testing method) and therefore not to be mistaken with a defect.

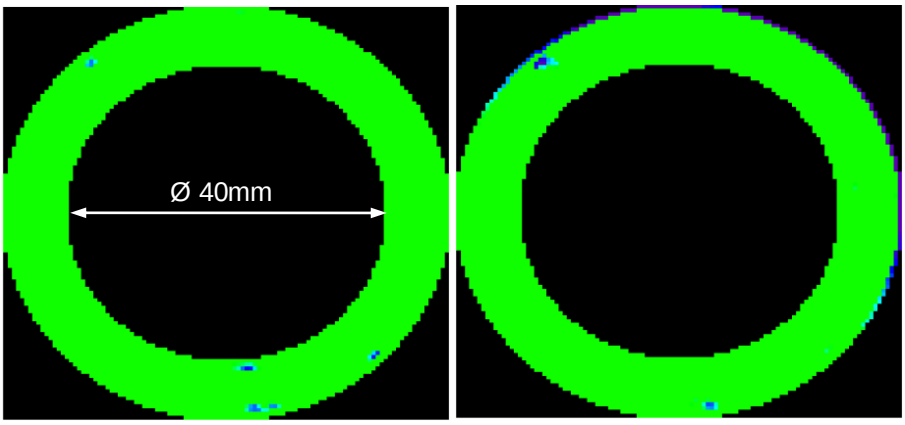

Figure 43: Ultrasonic scan of W-07 weld interface showing minor defects at inner/outer circumference before (left) and after (right) flash removal, defects are illustrated in blue

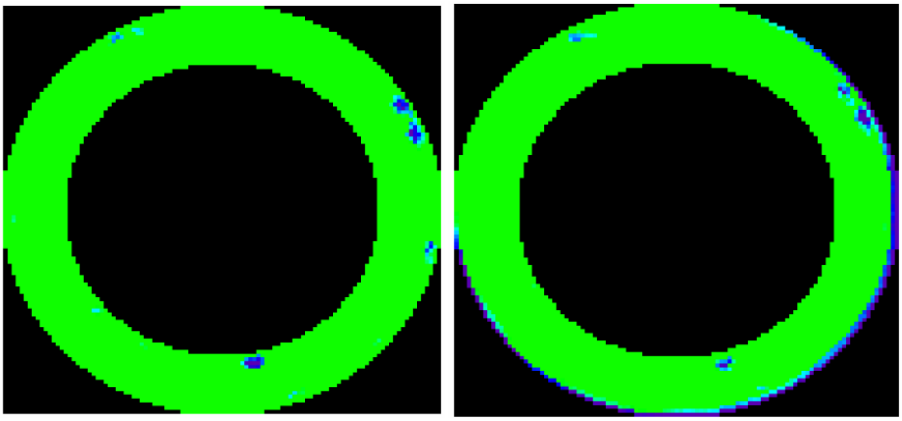

Figure 44: Ultrasonic scan of W-10 weld interface showing minor defects at inner/outer circumference before (left) and after (right) flash removal, defects are illustrated in blue

6.4 Penetrant test results (PT)

As shown in Figure 45, the welded specimens show defects scattered across the whole inner and outer circumference. Measurements (see Annex) show cracks up to 0.6 mm extension in tangential direction in the welding interface. As known from the existing inertia-drive process, cracks in the boundary areas should disappear after machining to the final dimensions. Therefore the original parts were tested again after a 1 mm chip-removal on the inner and outer diameter, as low as 5.5 mm wall thickness. However, cracks were still visible after machining the amount of cracks was significantly reduced. All cracks are located in the welding interface only. The defects on the Ø 60 mm shoulder (see Figure 45) were caused by the clamping device during machining, hence not to be associated to the welding process.

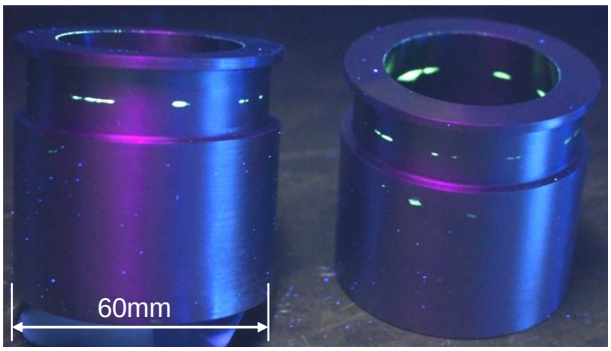

Figure 45: Penetrant inspection of specimen W-07 and W-10

This test was also conducted for the tensile test specimens as shown in Table 16 as well as for the raw material tensile samples (RL2-RRB 1, 2, 3). Two defect-free RRS samples out of weld assembly W-09 were identified. Furthermore two RRB samples passed the test, one out of weld assembly W-06 and one out of W-09. As assumed, no defects were detected with the three raw material samples (RL2-RRB 1, 2, 3).

Table 16: PT test of tensile test specimens (green dot = no defects)

ID	W-06	W-09
RRS	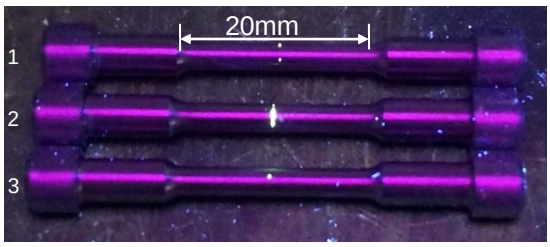	
RRB	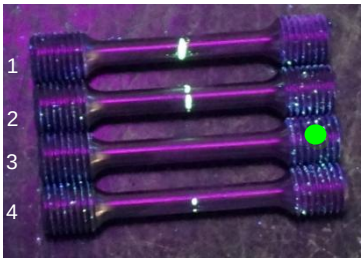	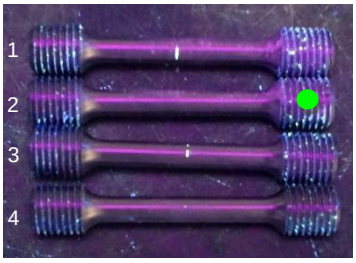

6.5 Hardness test results (HT)

The hardness profile of the weld cross section has been created for W-05 and W-08 and will be discussed together, due to the similarity of the results and the equality of the welding process (see Figure 46 and Figure 47).

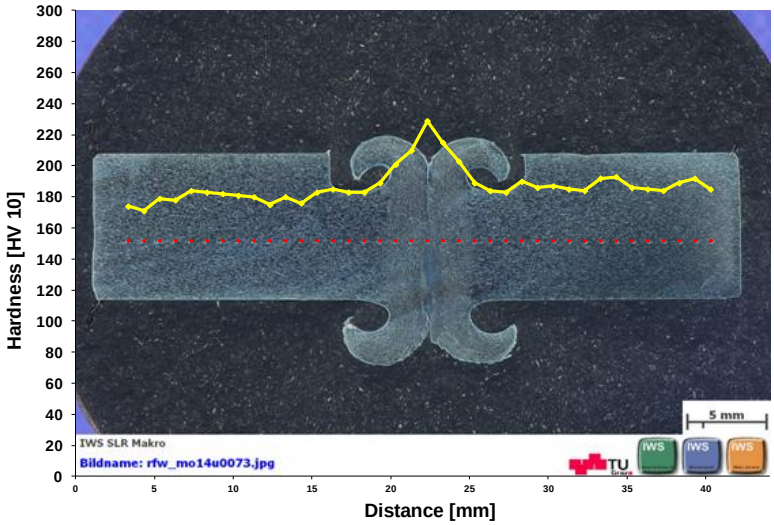

Figure 46: Hardness profile of W-05

The initial hardness of the TZM rod before welding was 259 HV (acc. to Plansee Inspection Certificate) while the welded parts (after post-weld heat treatment) showed a significant decrease to an average hardness of 188 HV10. The mean value in the base material after welding and post-weld heat treatment is approximately 180 HV10. The lowest single value was 170 HV10. An increase up to a maximum of 230 HV10 was observed in the weld zone.

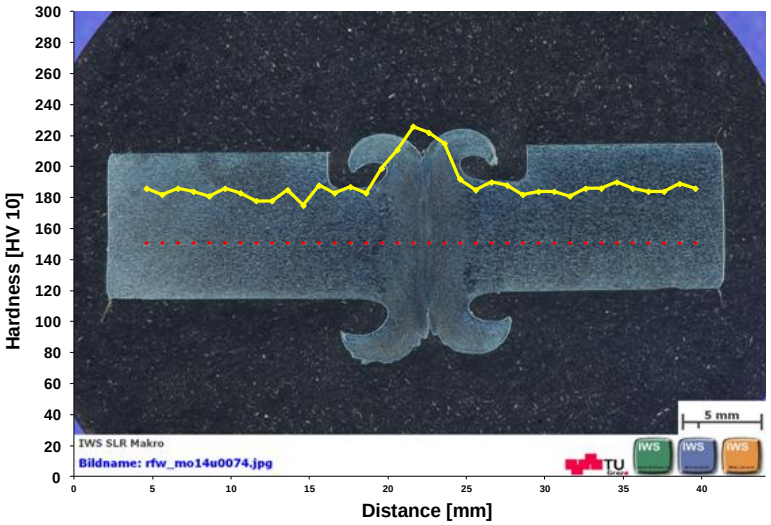

Figure 47: Hardness profile of W-08

The reduced hardness of the welded parts is caused by a change of the microstructure due to the PWHT and was also documented in Chapter 3.2.2.5.3. The hardness increase in the welding area can be traced back to the fine-grained microstructure caused by the forge force applied during the friction weld process.

The ratio between weld and base material equals to approximately 1.28. This means that the weld seam shows a 28% higher strength than the base material.

6.5.1 Hardness profile of tensile test specimens

Moreover, a hardness profile for one room-temperature and one elevated-temperature (1200 °C) tensile sample has been created, as shown in Figure 48 and Figure 49.

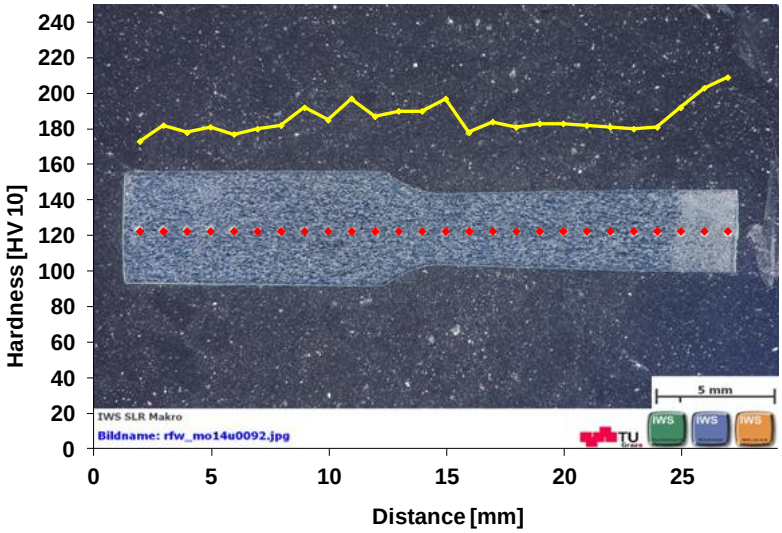

Figure 48: Hardness profile of room temperature tensile specimen W-06-RRS1

The minimum and average values of the brittle fracture room temperature sample are similar to the hardness measurements of the weld cross section described in the previous chapter. A slight decrease of the maximum hardness (located in the weld zone) from 230 HV10 to 210 HV10 was observed.

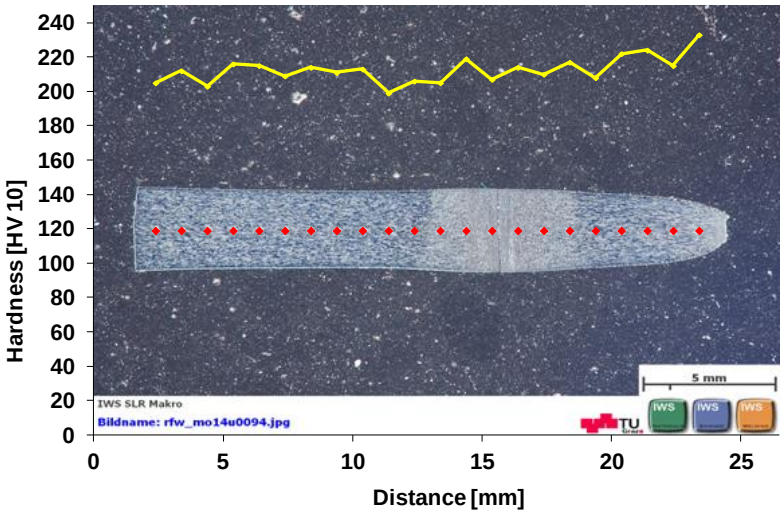

Figure 49: Hardness profile of high-temperature tensile specimen W-06-RRB3

The high-temperature tensile specimen which showed ductile fracture behavior in the base material has an average hardness of 213 HV10. The maximum value of 233 HV10 is located near the fracture. The increase of the average hardness in comparison to the welded specimen (and the brittle fracture sample) can be traced back to cold deformation[2] caused by the ductile fracture behavior.

6.6 Tensile test results (TT)

To avoid misunderstandings, it has to be remarked that the tensile tests for this study were only conducted for the raw material before welding and heat treatment (HT) as well as for the weld assemblies after PWHT. Therefore the common analogy between weld and base material cannot be drawn by evaluating the conducted tensile test results. However, comparable tensile test results for the raw material after HT were extracted from the Plansee Material Database and are documented in sub-chapter 6.6.2 for comparison.

[2] Cold deformation (work hardening) can occur up to a temperature of 1300°C for TZM acc. to an interview with Dr. Schatte (Plansee SE)

Table 17 gives an overview of all executed tensile tests with respect to the PT results. Due to cost and time issues, only one defective specimen was used for the high temperature test (containing one small punctiform defect determined in PT for W-09 RRB4).

Table 17: Tensile test results overview

Test temperature [°C]	ID	$R_{p0,2}$ [MPa]	R_m [MPa]	A_g [%]	A [%]	PT passed
22	W06_RRS 1	-	186	0.0	0.0	No
	W06_RRS 2	-	164	0.0	0.0	No
	W06_RRS 3	459	492	1.6	1.7	No
	W09_RRS 1	-	372	0.0	0.0	No
	W09_RRS 2	455	612	9.8	21.7	Yes
	W09_RRS 3	453	608	9.6	11.9	Yes
1200	RL2-RRB 1	375	390	0.6	15.1	Yes
	RL2-RRB 2	365	379	0.5	13.8	Yes
	RL2-RRB 3	352	375	0.6	13.9	Yes
	W-06 RRB 3	103	211	15.4	33.0	Yes
	W-09 RRB 2	103	211	14.9	35.1	Yes
	W-09 RRB 4	94	207	15,6	32,7	No

Macro-photos of all tensile specimens can be found in the Annex.

6.6.1 TT comparison for raw material before and after heat treatment

Figure 50 shows the ultimate tensile strength of the raw material before and after heat treatment (1550 °C for about 1.5 hours). The raw material shows an UTS of 765 MPa and a fracture elongation of 32% for the room temperature test. A decrease to 572 MPa accompanied by an increased fracture elongation of 46% was observed after heat treatment.

At a test temperature of 1200 °C the UTS of the raw material drops to 381 MPa and 14% fracture elongation. After HT a considerable decrease of the UTS to 205 MPa and an increase of the fracture elongation to 47% can be noted.

To sum up, the heat treatment leads to a decrease in strength and an increase in elongation at both test temperatures.

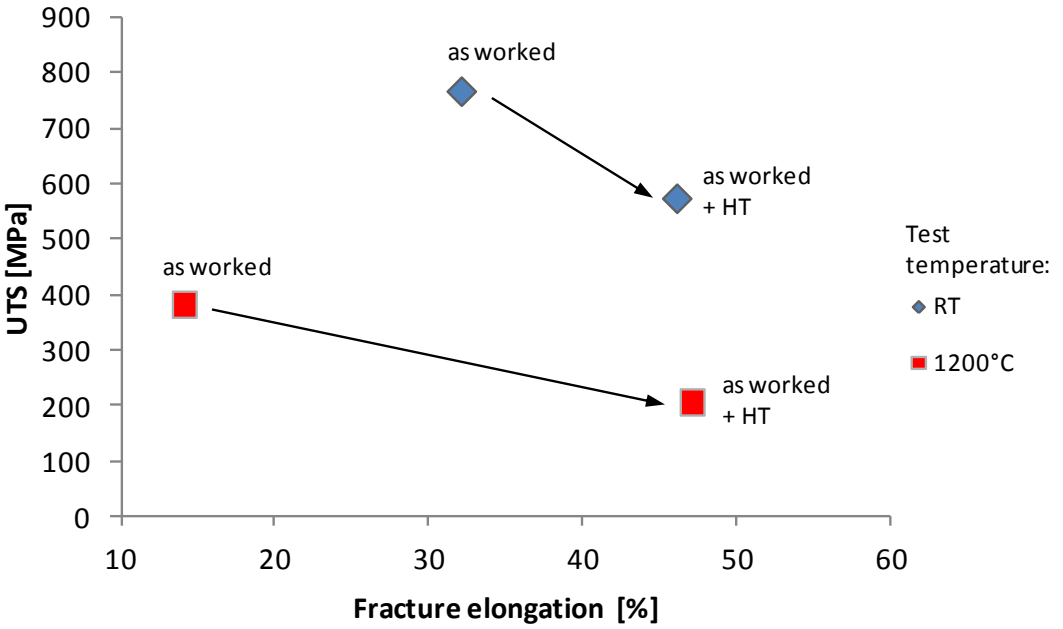

Figure 50: Ultimate tensile strength and elongation for raw material (as worked) before and after heat treatment (HT) at room and elevated test temperature; "as worked + HT" values are referenced from Plansee Material Database; "as worked" values are from the actual batch (Inspection Certificate & RL2-RRB 1,2,3 average)

6.6.2 TT comparison for raw material and welded specimens after HT

For ambient temperature test, brittle fracture behaviour and tensile strengths below 400 MPa were documented for the defective specimens (identified in the PT and UT test), whereas the defect-free specimens reached a mean ultimate tensile strength of about 610 MPa and a fracture elongation of 17% (see Figure 51 and Table 18).

At 1200 °C test temperature a significant decrease to 205 MPa is observed for the base material. The welded specimens have an ultimate tensile strength of 211 MPa with a fracture elongation of 34% (see Figure 51 and Table 18).

To conclude, the weld-assemblies show a slight increase in strength (these deviations are within the statistical spread). However, a considerable decrease of the fracture elongation was observed. The fracture for the brittle samples was located directly in the welding interface, whereas the fracture for the ductile samples was located in the base material, in the range of 3.2 to 9 mm next to the welding interface.

Table 18: Comparison of raw material and welded specimens TT results after heat treatment

Test temperature	Material condition	UTS [MPa]	Fracture elongation [%]
RT	as worked + HT (*)	572	46
	as welded + PWHT (**)	610	17
1200°C	as worked + HT (*)	205	47
	as welded + PWHT (***)	211	34

*Reference data from Plansee SE material database; ** average of W09_RRS 2 & W09_RRS 3, *** average of W-06 RRB 3 & W-09 RRB 2

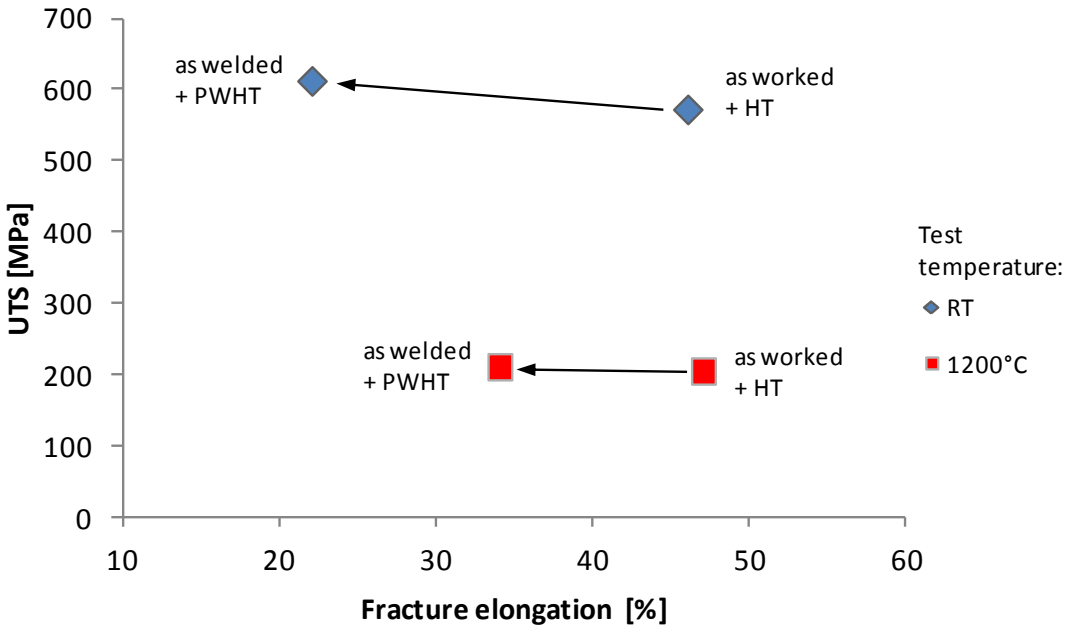

Figure 51: Ultimate tensile strength and elongation for base material (as worked + HT) and defect-free weld sample W-09 RRS 2 (as welded + PWHT) at room and elevated test temperature; variance to the other defect-free weld sample W09_RRS 3 negligible.

Figure 52 shows the engineering-stress-strain curves for the weld-specimen W-09 (RRS2 and RRB2) as well as for the base material at different test temperatures. For the tensile test at room temperature a technical elasticity limit of $R_{p0,2}$ = 455 MPa and a uniform elongation of 9.8% can be seen for the weld-sample. For the same weld-sample an UTS of 612 MPa and a fracture elongation of 22% were documented. In contrast, an elastic limit of 103 MPa and A_g=15 % were recorded for the high temperature test weld-sample. For 1200 °C test temperature the UTS equals to 211 MPa and the fracture elongation is 35 % for the weld-specimen.

By comparing the stress-strain curves at 22 °C test temperature a slight decrease of the uniform elongation and a significant decrease of the fracture elongation can be seen for the weld sample compared to the base material. Further, the stress-strain curves for the high-temperature test sample are quite similar. The only notable difference is again the previously discussed decrease in elongation for the weld-sample.

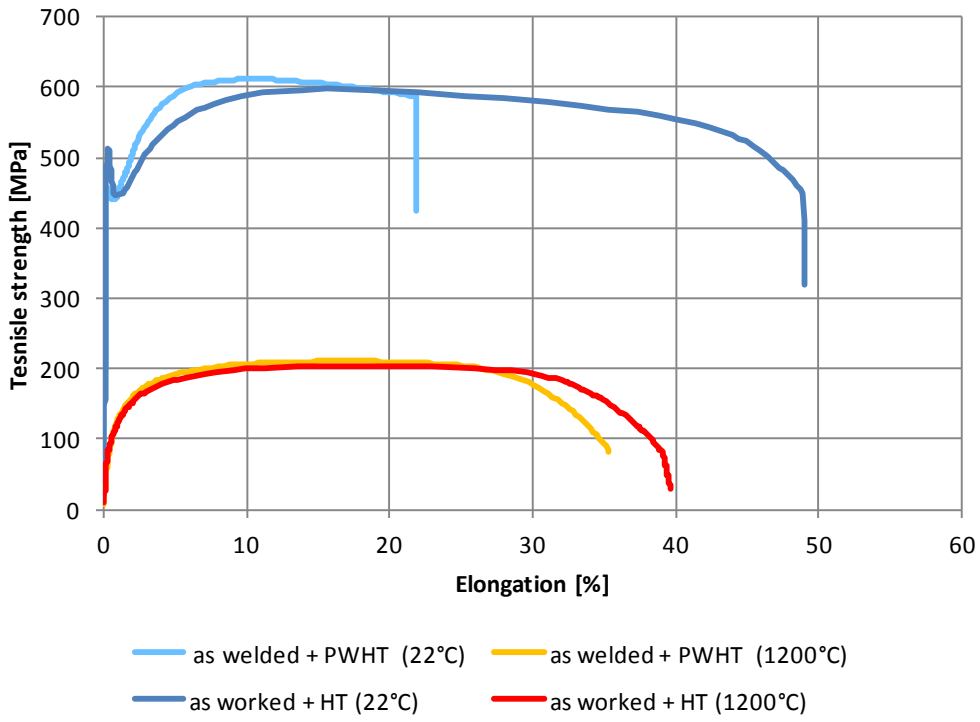

Figure 52: Engineering-stress-strain curve at room and elevated temperature for welded specimens (W-09 RRS2 & RRB2) after PWHT and comparable reference data (from Plansee Material Database) for the base material after HT

6.7 Metallography

Metallographic investigations were conducted for the raw material, the weld assemblies and the tensile test samples by means of light microscopy and SEM.

6.7.1 Microstructure specification of TZM rod

This investigation has been conducted for the specimen sampling as shown in Chapter 5.7.1.1., regarding the TZM rod base material before welding and post-weld heat treatment.

Figure 53 shows the metallographic cut in transversal direction of the TZM rod base material. The white and black etched areas show different grain orientations. Due to different cutting planes and dislocation densities, the etched surface is displayed lighter or darker[3]. It has to be remarked that TZM has a single-phase structure; hence the different grayscales should not be mistaken as different phases like it is known from typical steel micrographs. According to previous investigations[4] obviously observed grains detected with light microscopy were further divided when observed with a SEM. Therefore no clear statement concerning the grain boundaries can be made without additional SEM investigation. However, estimating the grain size according to [40] resulted in a mean grain size of approximately 30 µm (ASTM – G 7).

[3] Acc. to an interview with DI Mrotzek (Plannsee SE);
('the higher the dislocation density the darker etched surface')
[4] of Dr. Schatte (Plansee SE) acc. to an inteview

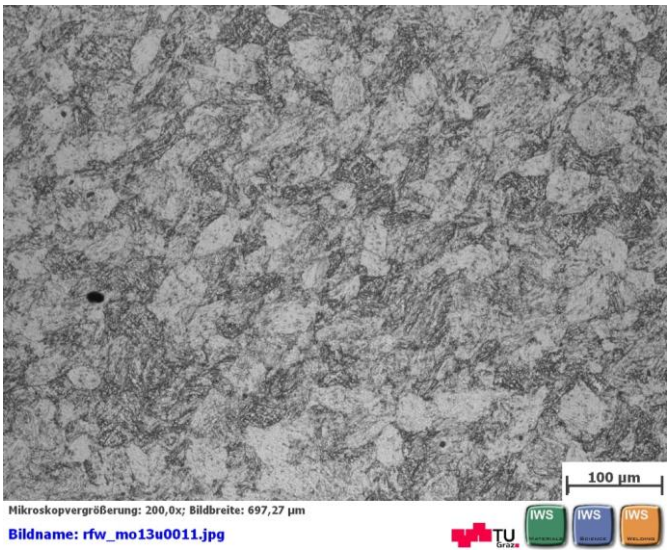

Figure 53: Microstructure of the TZM raw material in transversal direction (see Figure 40 for position of specimen 1 on semi-finished product)

Figure 54 shows the longitudinal view of the TZM rod base material. The elongated microstructure, which is characteristic for the manufacturing process, demonstrates a high degree of deformation in the range of 75% (area reduction). Furthermore the direction of deformation can be seen. The slight nonparallel orientation of the stretched areas is also a characteristic of the forging process. In conformity with the intentions of the manufacturing process no recrystallized grains were detected.

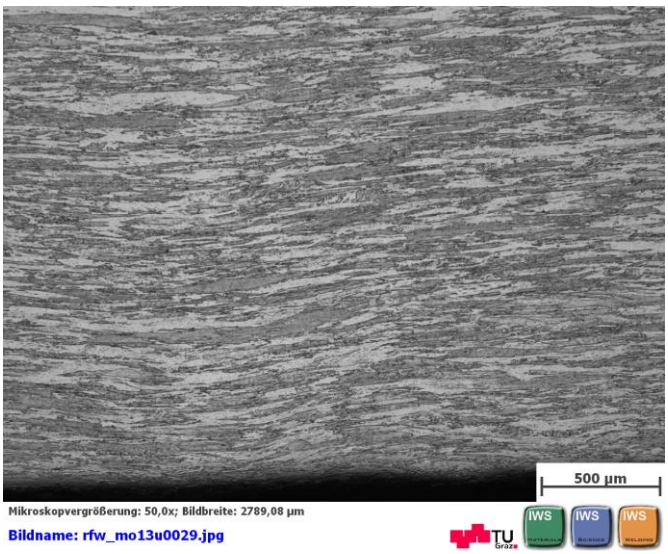

Figure 54: Microstructure of the TZM raw material in longitudinal direction (see Figure 19 for position of specimen 3 on semi-finished product)

6.7.2 Microstructure specification of welded TZM parts

Figure 55 gives an overview of the welding area. As characteristic for this welding process, different grain deformations can be seen across the weld zone. The heat input and the applied force leads to a fine-grained micro structure in the weld zone. At approximately three millimetres from the welding interface the transition to a more coarse grained structure can be seen. The micrographs let assume a recrystallized structure of the base material caused by the post-weld heat treatment. This observation is supported by the results of hardness measurements and tensile testing.

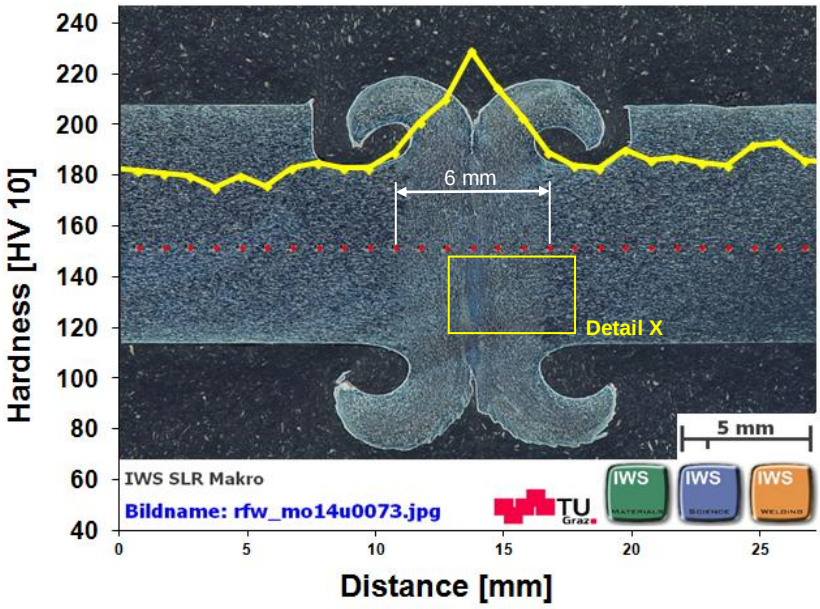

Figure 55: Specimen W-05:
Visible HAZ of 6 mm, location of detail X (see Figure 56), hardness profile of weld interface

Figure 56: Transition between HAZ and base material, welding area of specimen W-05 – Detail X

The micrographs in combination with the hardness measurements lead to the determination of a visible HAZ width of about 6 millimetres (see Figure 55).

6.7.3 Microstructure specification of tensile test specimens

Figure 57 shows the microstructure of a room-temperature tensile specimen. By comparing with the previous investigations (e.g. HAZ with of approximately three hardness measurement dots which equals to approximately three millimeters), the fracture is supposed to be located directly in the welding interface. Macro-photos of the tensile specimens can be found in the Annex.

Figure 57: Micrograph of room-temperature tensile specimen W-06-RRS1

Although the fracture from the high-temperature tensile test was located in the base material, the sample broke during microstructure specimen preparation directly in the welding interface, as shown in Figure 58.

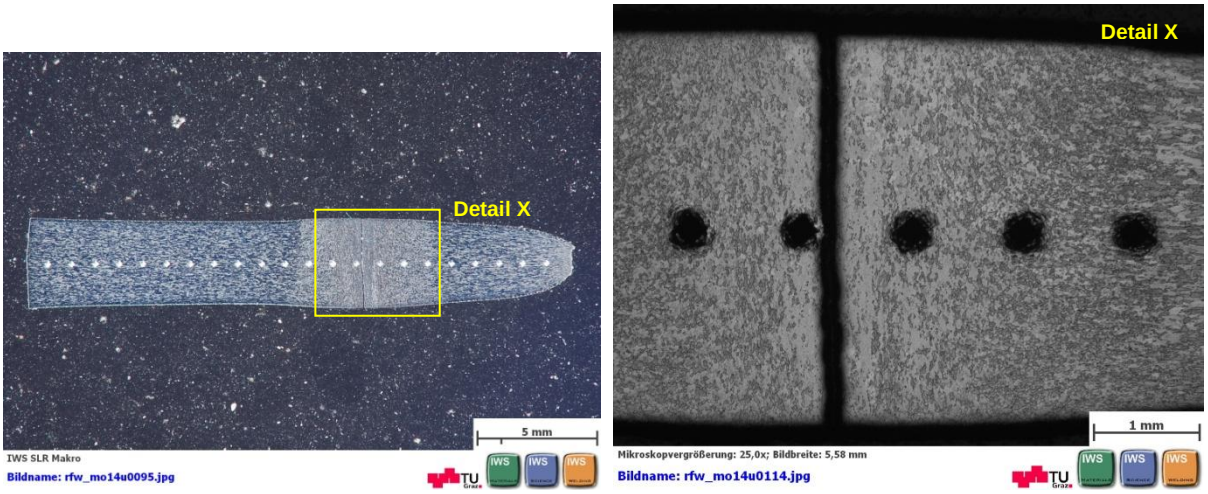

Figure 58: Micrograph of high-temperature tensile specimen W-06-RRB3

6.7.3.1 EDX of weld zone

Additionally, EDX investigations in the weld zone of W-05 were executed. Therefore two spot scans, one located in the matrix and one located on a precipitate were created (see Figure 59).

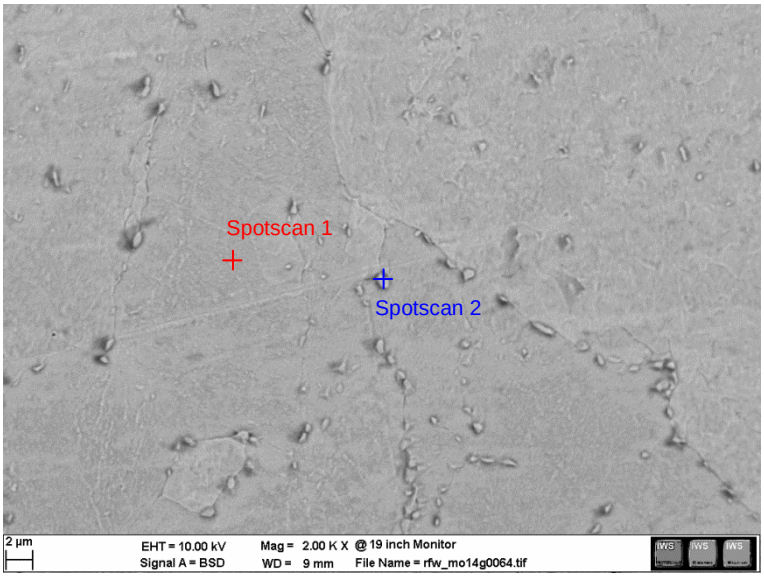

Figure 59: Location of spot scan 1 (base material) and 2 (precipitate) on TZM weld assembly W-05

In Figure 60 the EDX spectrum of TZM is documented for the two spots described above: The typical elements molybdenum, titan, zircon as well as oxygen were detected. When comparing the two spots, a minor decrease of oxygen and molybdenum for spot 2 (precipitate) can be seen. However, due to the small size of the precipitates (<1µm) in relation to the excitation volume, the matrix is still partly included in the record of spot scan 2, and therefore no quantitative statement concerning the exact composition of the precipitate can be made. Nevertheless, a significant increase of titan was observed for spot 2. In alignment with the literature review (see 3.2.2.6) the micrographs let assume the location of the particles on (sub-) grain boundaries or former grain boundaries. Typically Mo_2C carbides (on former grain boundaries) or (Mo-)Ti mixed carbides (on the sub grain boundaries) were documented [29]. However, the distinctive increase of Ti could indicate a molybdenum-titan-carbide. To support this assumption further investigations (e.g.: Hasson-color-etching) should be executed.

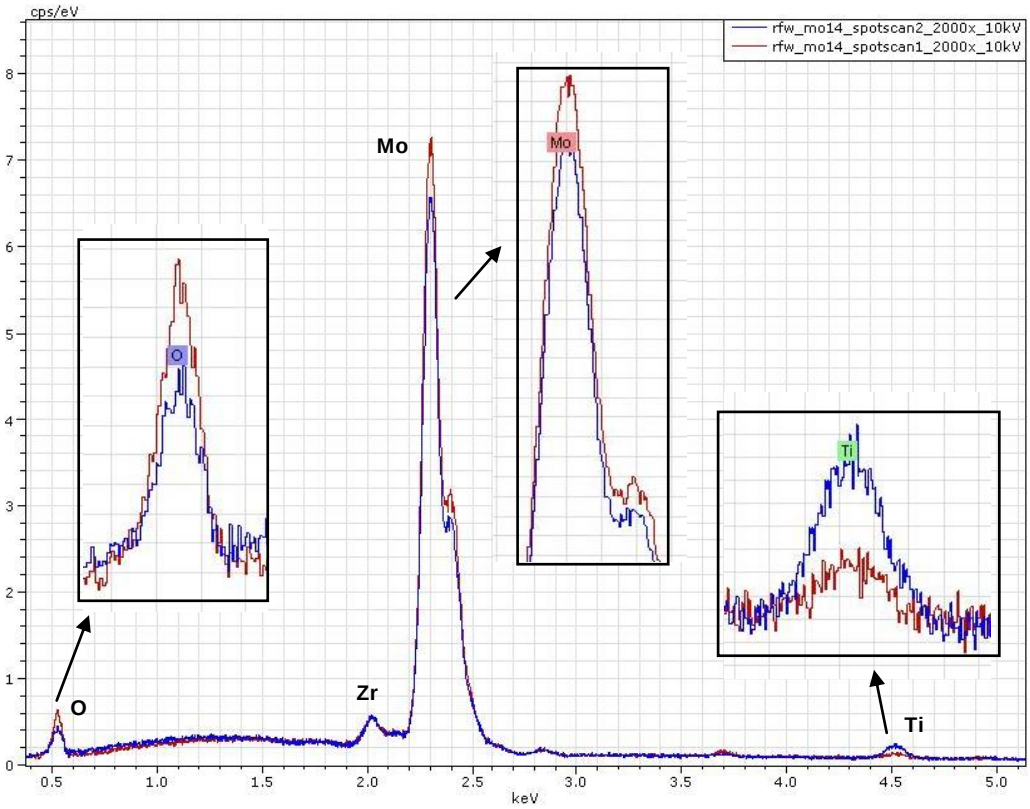

Figure 60: EDX scan for TZM weld assembly W-05 showing the two spot scan 1 on matrix (Red) and spot scan 2 on precipitate (Blue)

6.7.4 Fracture surface of tensile test specimens (SEM)

Figure 61 shows the fracture surface (located in the welding interface) of the RT tensile specimen W-06 RRS2. A brittle fracture surface with two slightly different sectors can be seen. Detail X shows a typical intergranular fracture surface. This occurrence is not that much distinct in detail Y were marginal transgranular fracture surfaces can be identified.

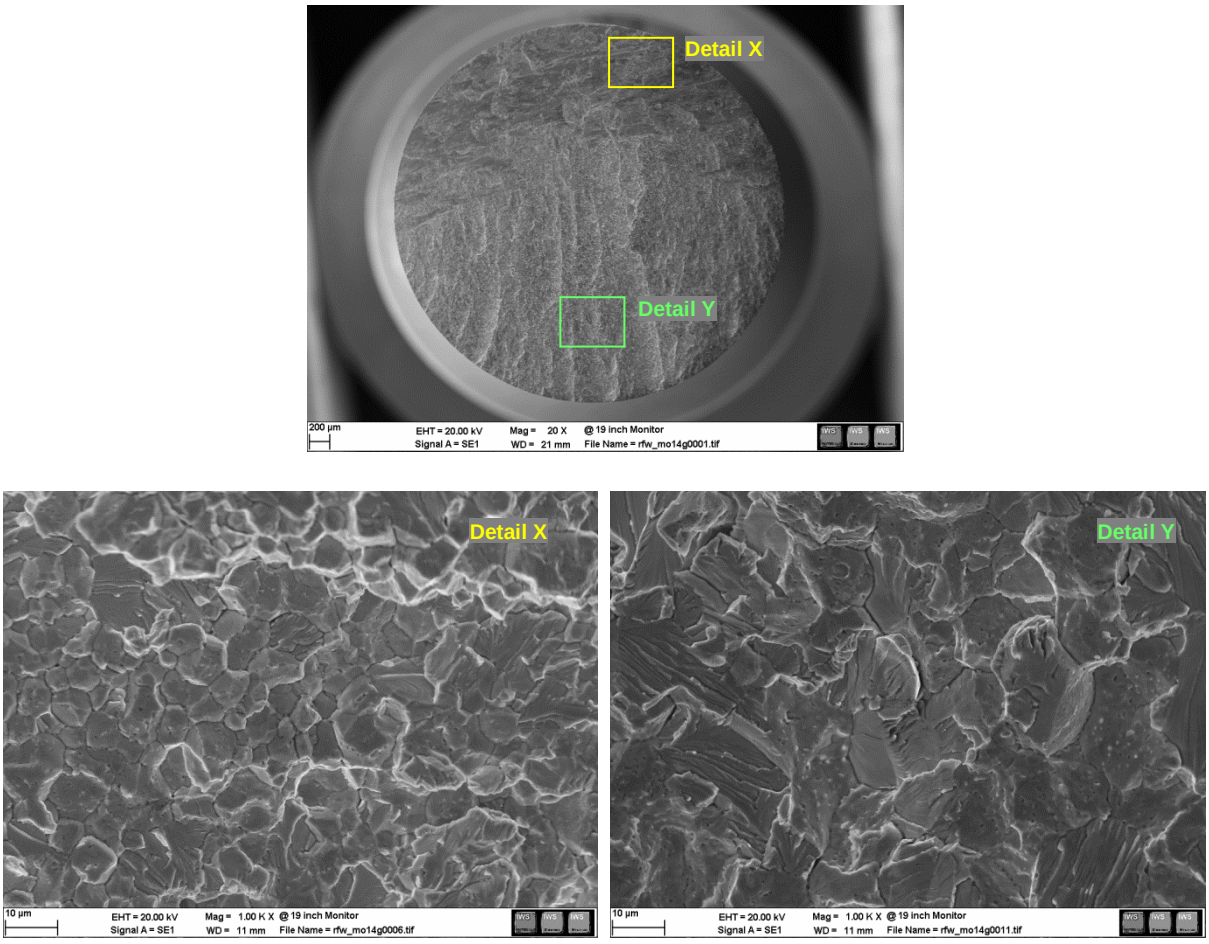

Figure 61: Brittle fracture surface and Detail X & Y for room temperature tensile specimen W-06 RRS2

In contrast, Figure 62 shows a typical ductile fracture surface for TZM room-temperature tensile samples. The fracture is located in the base material approximately 3.2 mm next to the welding interface. In specimen W-09 RRS2 no more original grain formations can be seen, due to mere transgranular fracture behavior.

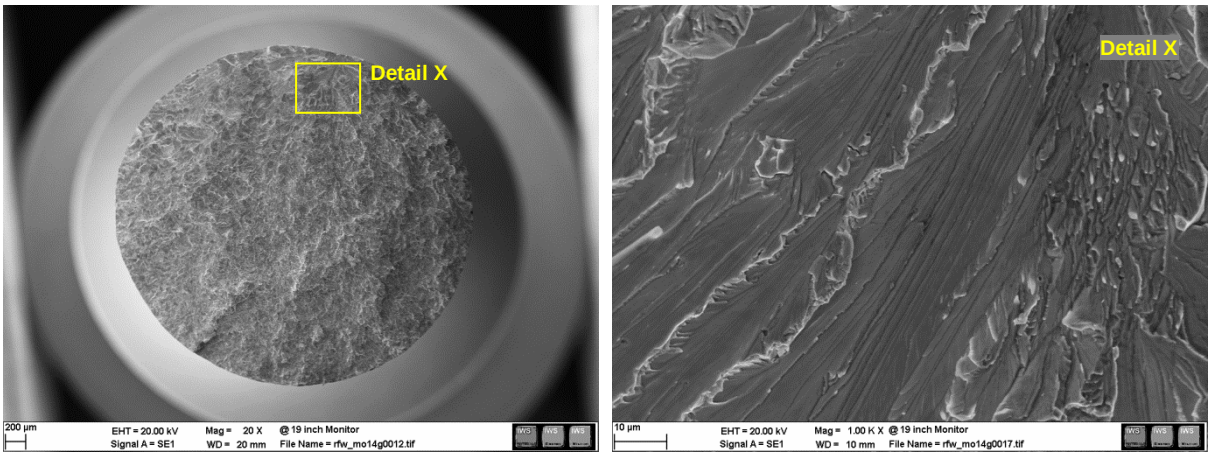

Figure 62: Ductile fracture surface and detail X for room-temperature tensile specimen W-09 RRS2

Figure 63 shows the fracture surface of a high temperature tensile specimen. The fracture is located in the base material approximately 9 mm next to the welding interface. The honeycomb structure is a typical appearance in purely ductile fracture behavior. The flat surface can be traced back to mechanical damage which occurred during dismounting the sample from the clamping device.

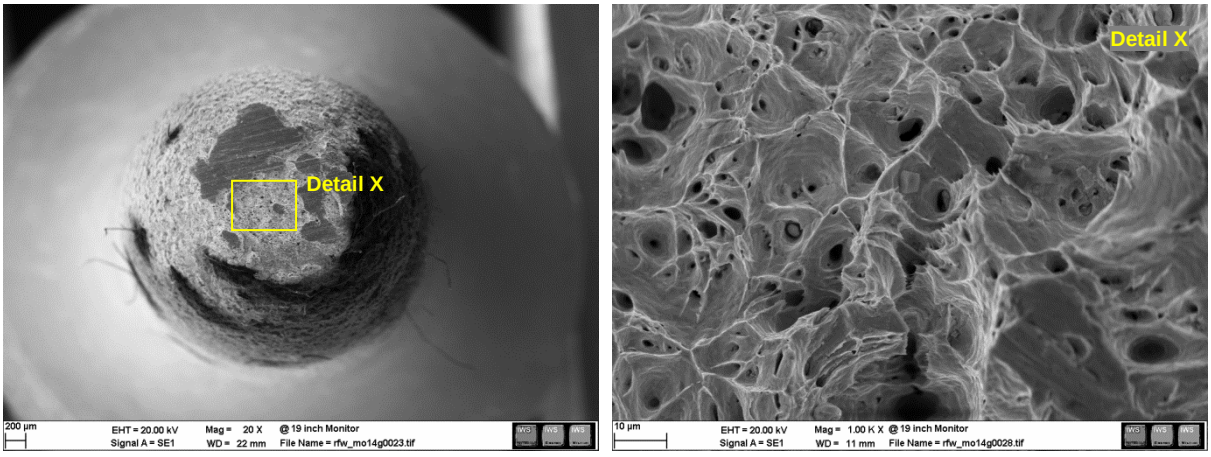

Figure 63: Ductile fracture surface and detail X for 1200°C tensile specimen W-09 RRB2

6.8 Flash formation

A cross section of the flash formation on the pipe wall is illustrated in Figure 64. It has to be remarked that this is only a random spot check; hence variations across the circumference of the weld sample are possible.

The first overall impression of the macro inspection is quite satisfying. As already documented in chapter 6.1 an evaluation according to DVS 2909-5 (for steel-material) shows a proper flash-shape and no surface cracks. Additionally, the weld cross-section is greater than the initial cross-section, whereby another quality criterion is fulfilled. Even if not quite comparable, investigations of [41] on the proper flash formation in linear friction welding show, that the flat butt (see Detail X) is a conspicuous feature, which may indicate an inadequate bond, caused by too less heat input and/or too less forge force.

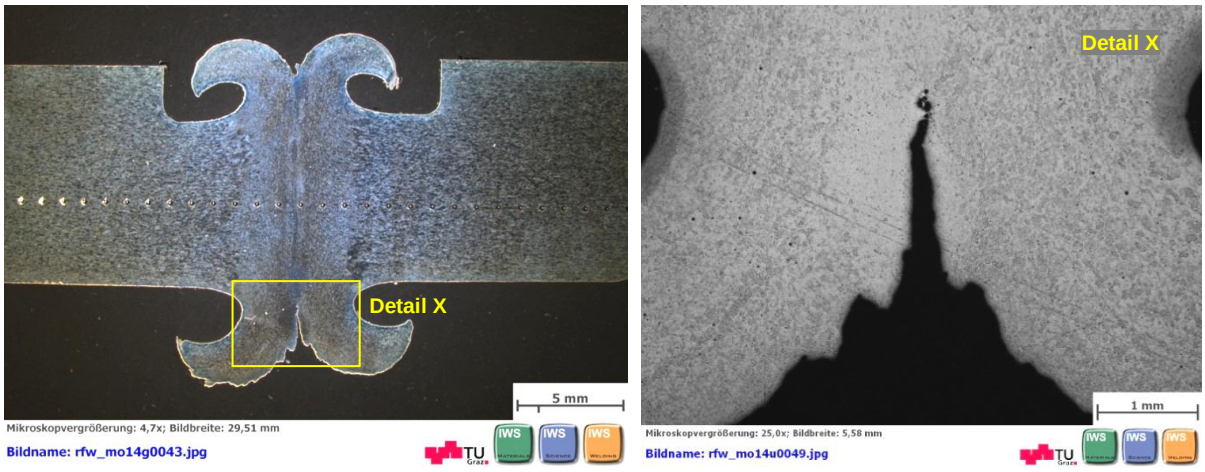

Figure 64: Flash formation on the pipe wall with Detail X

6.9 Defective weld specimens

Before accomplishing the first proper welding results, several iterative steps were necessary to find the appropriate machine settings. Problems like the incorrect amount of clamping force (see Figure 65 / W-01) and the power limit of the electric motor resulted in multiple defective bonds. As shown in Figure 65, these welds did not show an adequate flash formation. Due to a lack of heat input into the welding interface, the necessary parameters for a proper weld were not reached. After breaking these parts by applying very low force (bench vice and hammer), the welding interface has been examined, showing only a point-wise bond of the two parts.

Figure 65: Defective welds

7 Summary

This study was executed within bilateral collaboration between PLANSEE SE and the Institute for Materials Science and Welding at Graz University of Technology. Direct-drive friction welding was done by Klaus Raiser GmbH, Germany, an external contractor with over 30 years of experience in friction welding.

In this study the potential of direct-drive friction welding for tubular TZM components was investigated. An energy input of 33 W/mm² was applied on a cylindrical specimen with OD55 mm and a wall thickness of 7.5 mm with a preheat temperature of about 400 °C. This energy input was achieved by applying 63 MPa friction pressure at a constant speed of 1500 rpm for three seconds.

Visual testing revealed a proper flash formation without irregularities or cracks. Minor defects identified in the circumferential areas detected with ultrasonic and dye penetration test may have been caused by the limited heat input. In compliance with the performed theoretical considerations a higher heat input was intended, but could not be realised with the available machine.

Microstructural investigation showed a fine-grained microstructure in the welding area. The micrographs in combination with the hardness measurements show a visible HAZ width of about 6 millimetres. Further, the hardness profile across the welding area shows a ratio between weld and base material of ~1.28. This means that the weld seam shows a 28% higher ultimate tensile strength than the base material.

The tensile test results at room and elevated temperature of the successfully welded samples are characterised by a slight increase of the UTS (traced back to scattering) and a considerable decrease of the fracture elongation, compared to the base material. As desired, the fracture for the defect-free weld samples was located in the base material and not in the welding area. On the other hand, the defective specimens, identified in the PT and UT test, showed brittle fracture behaviour and tensile strengths below 400 MPa.

To sum up, the feasibility of direct-drive friction welding of tubular TZM-components was proven. However, it has to be remarked that due to the limited number of samples only one parameter set was applied for all welding experiments. Therefore an optimization potential can be assumed and further research is still required.

8 Outlook

As a next step towards the integration into the industrial production process a systematic parameter optimization with respect to strength and toughness should be carried out to ensure the specified values. An adaption (down-sizing) of the specimen geometry to minimize costs and/or to compensate limited machine capacity should be considered. Further, meaningful specific parameter combinations (e.g. power density) should be determined to support the transferability of the findings to other specimen geometries. For reasons of efficiency, further improvements such as a three-stage friction welding process should be considered for preheating instead of heating the parts in a furnace.

Furthermore the influence of the current PWHT could be analyzed and if necessary optimized, e.g. by splitting the weld specimens and annealing at different temperatures. Additionally, the tensile test results for the base material after PWHT for the same charge material should be investigated to support a proper weld qualification.

Moreover, an adaption of the sample geometry to the final product should be performed by conducting a tube-to-plate bond instead of a tube-to-tube bond.

List of figures

List of tables

References

[1] J. A. Shields, “Applications of Molybdenum Metal and its Alloys”, *Int. Molybdenum Assoc. www.imoa.info*, 2013.

[2] B. Tabernig and N. Reheis, “Joining of molybdenum and its application”, *Int. J. Refract. Met. Hard Mater.*, vol. 28, no. 6, pp. 728–733, Nov. 2010.

[3] M. Maalekian, “Friction welding – critical assessment of literature”, *Sci. Technol. Weld. Join.*, vol. 12, no. 8, pp. 738–759, Nov. 2007.

[4] A. Ambroziak, “Friction welding of molybdenum to molybdenum and to other metals”, *Int. J. Refract. Met. Hard Mater.*, vol. 29, no. 4, pp. 462–469, Jul. 2011.

[5] H. Kestler, “Joining of Refractory Metals”, *ASM Handb. Int.*, vol. Vol 7.

[6] N. Reheis, B. Tabernig, H. Kestler, L. S. Sigl, D. de Pretis and N. Enzinger, “Friction Welding of TZM Components”, *Tungsten, Refract. Hardmaterials Conf. Orlando - USA*, 2014.

[7] N. Enzinger, “Lecture-notes: Advanced Processing Technologies 335.002 SS 2013, TU Graz.”

[8] J. Tändl, “Friction stir welding of multilayered steel; Master Thesis, TU Graz”, 2012.

[9] A. CAN, M. ŞAHİN and M. KÜÇÜK, “Modelling of friction welding”, *Unitech Gabrovo*, 2010.

[10] I. V. Kragelski and I. A. Vinogradioa, “Coefficient of friction”, *Mashgiz*, 1962.

[11] M. B. Hollander, C. J. Cheng and J. C. Wyman, “Friction Welding Parameter Analysis”, *Weld. J. Res. Suppl.*, p. 495s–501s.

[12] A. S. Gelman and M. P. Sander, “Mechanisms of friction”, *Weld. Prod.*, pp. 53–61.

[13] V. I. Vill, “Friction welding of metals”, *New York, Am. Weld. Soc.*, 1962.

[14] PLANSEE, “Website”, 2013. [Online]. Available: http://www.plansee.com/en/Materials-Molybdenum-402.htm. [Accessed: 20-Nov-2013]

[15] P. W. Lee, Y. Trudel, R. Iacocca, R. M. German, B. L. Ferguson, W. B. Eisen, K. Moyer, D. Madan and H. Sanderow, “Refractory Metals”, vol. 7, pp. 903–913, 1998.

[16] “CES EduPack, Version 2013.” Granta Design Ltd.

[17] PLANSEE, “Molybdän Werkstoffeigenschaften und Anwendungen Molybdenum Material Properties and Applications Molybdän Molybdenum”, *Info folder*, 2013.

[18] J. Warren, “The 700 ° C tensile behavior of Mo-OSTi-O . O8Zr-0 . 02X (TZM) extruded bar measured transverse and parallel to the billet extrusion axis”, vol. 4368, no. 98, 1998.

[19] B. V. Cockeram, “The mechanical properties and fracture mechanisms of wrought low carbon arc cast (LCAC), molybdenum–0.5pct titanium–0.1pct zirconium (TZM) and oxide dispersion strengthened (ODS) molybdenum flat products”, *Mater. Sci. Eng. A*, vol. 418, no. 1–2, pp. 120–136, Feb. 2006.

[20] Y. Hiraoka, “Development of MO alloys with improved resistance to embrittlement by recrystallization and irradiation”, vol. 5, no. 96, 1996.

[21] C. Schimpf, “Characterisation of thermally activated deformation processes in the Molybdenum alloy TZM”, 2006.

[22] A. J. Mueller, R. Bianco and R. W. Buckman, “Evaluation of oxide dispersion strengthened (ODS) molybdenum and molybdenum - rhenium alloys”, vol. 18, no. 2000, 2001.

[23] L. S. Sigl, A. Hoose and R. Schiftner, “Crack Resistance of the Molybdenum Alloys TZM and MHC at Ambient and Elevated Temperatures”, vol. 1, pp. 1–9, 2009.

[24] C. Wüstefeld, T. Mrotzek, A. Hoffmann, M. Beschliesser and U. Martin, “Creep Behaviour and Microstructure of Molybdenum Alloys at High Temperatures.”

[25] B. Fischer, S. Vorberg, R. Völkl, M. Beschliesser and A. Hoffmann, “Creep and tensile tests on refractory metals at extremely high temperatures”, *Int. J. Refract. Met. Hard Mater.*, vol. 24, no. 4, pp. 292–297, Jul. 2006.

[26] W. Martienssen and Warlimont H., “Springer Handbook of Condensed Matter and Materials Data.” 2005.

[27] T. Mrotzek, A. Hoffmann and U. Martin, “Work Hardening of the Molybdenum Alloy”, *Present. Plansee Semin.*, 2009.

[28] T. Mrotzek, “Mikrostruktur und Verformungsverhalten der Molybdänlegierung TZM”, *PAG Abschluss*, 2006.

[29] T. Mrotzek, a. Hoffmann and U. Martin, “Hardening mechanisms and recrystallization behaviour of several molybdenum alloys”, *Int. J. Refract. Met. Hard Mater.*, vol. 24, no. 4, pp. 298–305, Jul. 2006.

[30] H. Seli, A. I. M. Ismail, E. Rachman and Z. A. Ahmad, “Mechanical evaluation and thermal modelling of friction welding of mild steel and aluminium”, *J. Mater. Process. Technol.*, vol. 210, no. 9, pp. 1209–1216, Jun. 2010.

[31] *AWS C6.2/C6.2:2006 - Specification for Friction Welding of Metals*.

[32] “DVS standard (2909, Part 3), German: Reibschweißen von metallischen Werkstoffen”, *Deutscher. Verband für Schweißtechnik*, 1994.

[33] DIN EN 583, Non-destructive testing - Ultrasonic examination., 1998

[34] Reuter, “Einführung in die Ultraschallprüfung”, *Fh HH, Werkstoffprüfung Einführung die Ultraschallprüfung*, pp. 1–12.

[35] USRA.de, “Schematic ultrasonic picture.” [Online]. Available: http://www.usra.de/category/tags-buch/nahfeld. [Accessed: 16-Apr-2014].

[36] ÖNORM EN 571 - Non destructive testing - Penetrant testing.

[37] ISO 6507-1:2005 Metallic materials -- Vickers hardness test -- Part 1: Test method.

[38] DIN EN ISO 6892:2009-12 (E). Metallic materials - Tensile testing - Method B.

[39] C. Pöhl, J. Schatte and H. Leitner, “Metallographic characterization of the molybdenum based alloy MHC by a color etching technique”, *Mater. Charact.*, vol. 77, pp. 63–69, Mar. 2013.

[40] ASTM E112 - 13 Standard Test Methods for Determining Average Grain Size.

[41] K. Mucic, N. Enzinger and F. Fuchs, “Linear Friction Welding of High Strength Chains”, in *Trends in Welding Research: proceedings of the 9th international conference*, 2013, pp. 752–756.

Annex

8.1 Course of action overview

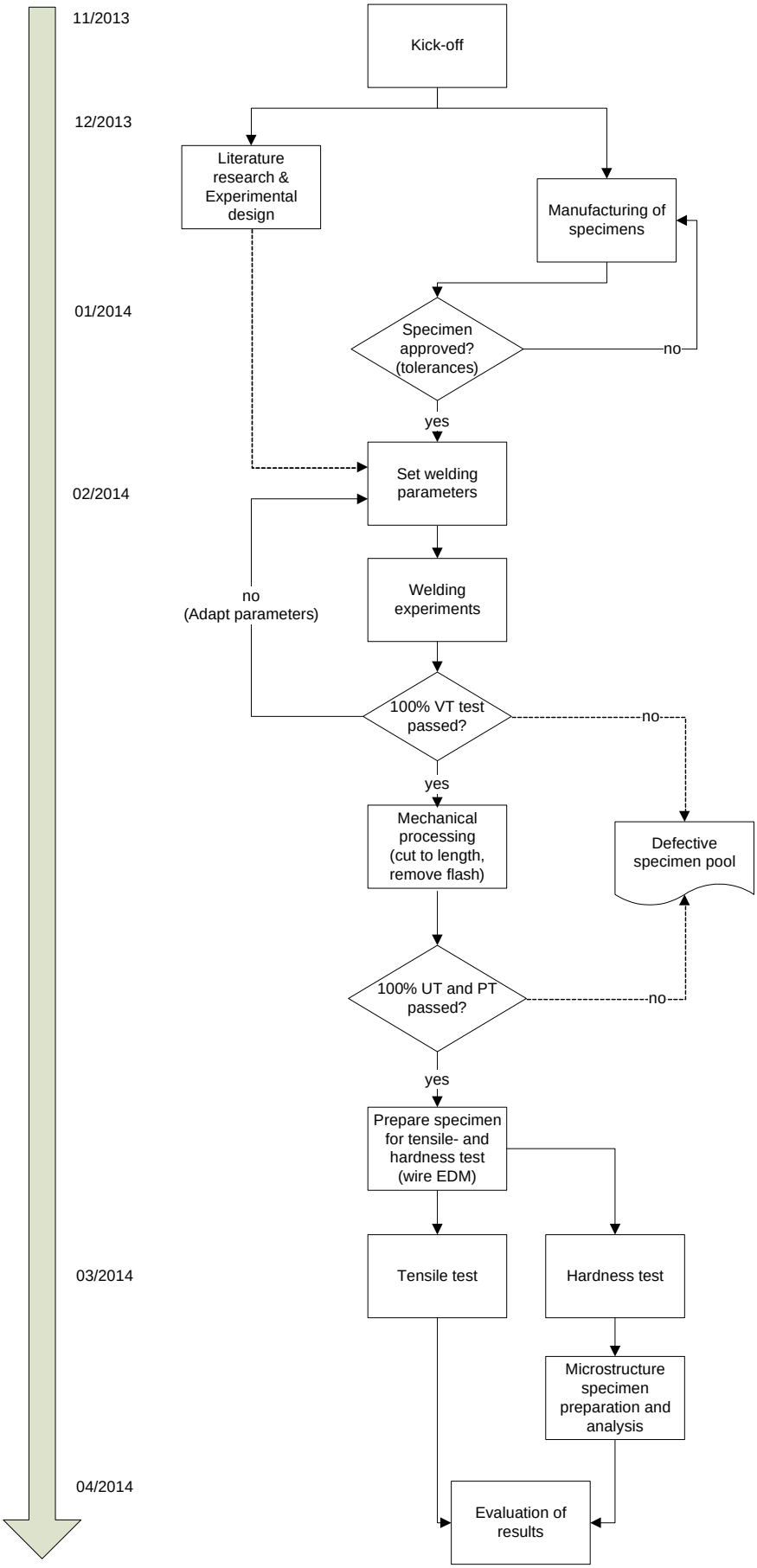

8.2 Inspection certificate

PLANSEE SE
A - 6600 Reutte
Tel: +43/5672/600-0
Fax: +43/5672/600-500
http://www.plansee.com

PLANSEE

RoHS QUALIFIED
quality austria
SYSTEM CERTIFIED
ISO 9001:2008 NR. 02175/1
ISO 14001:2004 NR. 01031/1
OHSAS 18001:2007 NR. 00301/1

INSPECTION CERTIFICATE
acc. to DIN EN 10204 - 3.1

Report No.:	790000071856
Date:	22.10.2013
Customer:	PLANSEE intern / ISTV
PLANSEE-Order No./Pos.No.:	
PLANSEE-Material-No.:	239897
PLANSEE-Segment / PoC. / ☎	
Customer Order No.:	
Specification No.:	PS-IHR-101
Material / Product:	TZM - ROD
Condition of material / Quality	/
Dimensions:	dia 70 x 2600 mm
Quantity / Weight:	102 kg
Batch(es):	0090998840

GUARANTEED CHEMICAL COMPOSITION: (determined in QA-QR-06-01)

Mo	Balance	Ti	0,40 - 0,55 %	Zr	0,06 - 0,12 %
Al	max. 10 µg/g	Cr	max. 20 µg/g	Cu	max. 20 µg/g
Fe	max. 20 µg/g	K	max. 20 µg/g	Ni	max. 10 µg/g
Si	max. 20 µg/g	W	max. 300 µg/g	C	100 - 400 µg/g
H	max. 10 µg/g	N	max. 10 µg/g	O	max. 500 µg/g
Cd	max. 5 µg/g	Hg	max. 1 µg/g	Pb	max. 5 µg/g

Cr(VI) + Organic impurities (e.g. PBB, PBDE, PFOS, PFOA)*

The requirements of the EU-diretives 2002/95/EG, 2000/53/EG and 2006/122/EG for the restriction of hazardous substances (RoHS) are fulfilled.

*) The presence of Cr(VI) and organic impurities can be excluded definitely because of the production process (multiple heat treatment at temperatures above1000°C in H2-atmosphere).

ACTUAL CHEMICAL BATCHANALYSIS:

O	=	225 µg/g	Ti	=	4423,8 µg/g
Zr	=	708,0 µg/g	C	=	363,6 µg/g

MECHANICAL PROPERTIES:

0,2 % Yield stress	EN ISO 6892-1/Methode B:	771 MPa
Ultimate tensile strength	EN ISO 6892-1/Methode B:	765 MPa
Percentage elongation	EN ISO 6892-1/Methode B:	24,1 %
Hardness HV	EN ISO 6507-1:	259
Density	EN ISO 3369:	>10,10 g/cm³
100% Ultrasonic tested		

Certified that the supplies/services detailed hereon have been inspected and tested in accordance with the conditions and requirements of the contract or purchase order and unless otherwise noted below, conform in all respects to the specification(s), drawing(s) relevant thereto.
This certificate has been generated by computer and need not to be signed for validity according to EN 10204.

PLANSEE SE
High Performance Materials
Inspection Department QM

Authorized inspection representative

(Partner) (Lutz)

Material Identification

Project	Friction Welding, TU – Graz, D. de Pretis
Material	TZM
Material Nr.	239897
Lot Nr.	0090998840
Dimensions	Ø70 x 1990mm (Rod 1), Ø70 x 600mm (Rod2)
Weight	78 / 24 Kg
Sample ID	FWT-01, FWT-02,……FWT-44
Date	27.11.2013

TZM-Rod 1

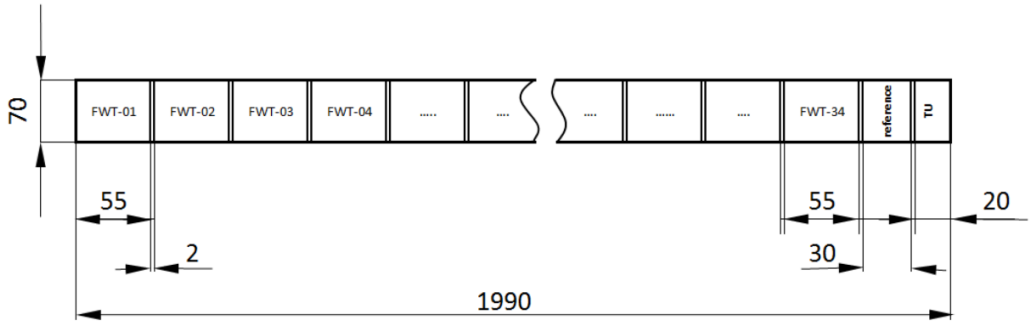

TZM-Rod 2

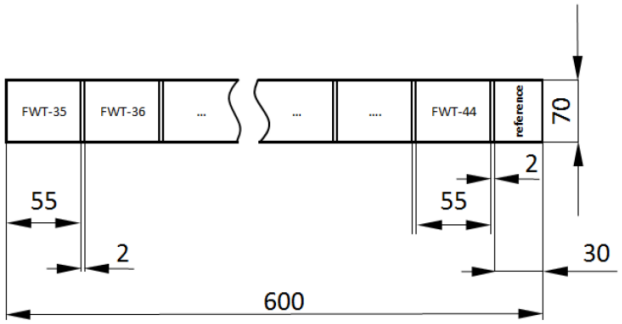

PLANSEE

Fig.1 Photograph of forged TZM – rods prior to machining to final friction weld samples

Fig.2 Details of Material Identification for TZM – rods1/2

8.4 Post weld heat treatment protocol

Fahrtenprotokoll HVLX_1

Programm: Tassenglühung 1600/90 Fahrt Nr.: X1-005-14

	Programmabschnitt	Dauer [hh:mm:ss]	°C	mbar	Digitalspur 1 2 3 4 5 6 7 8 9 10 11 12 13 14 15 16
0	Initialschritt	00:00:03	20.0		1
1	HOCHVAKUUM	01:00:00	800.0		1 1
2	HOCHVAKUUM	02:00:00	1550.0		1 1
3	HOCHVAKUUM	01:30:00	1550.0		1 1
4	HV ABKUEHLEN	00:45:00	500.0		1
5	N2 ABKUEHLEN	00:01:00	50.0	600	1 1
6					
7					
8					
9					
10					
11					
12					
13					
14					

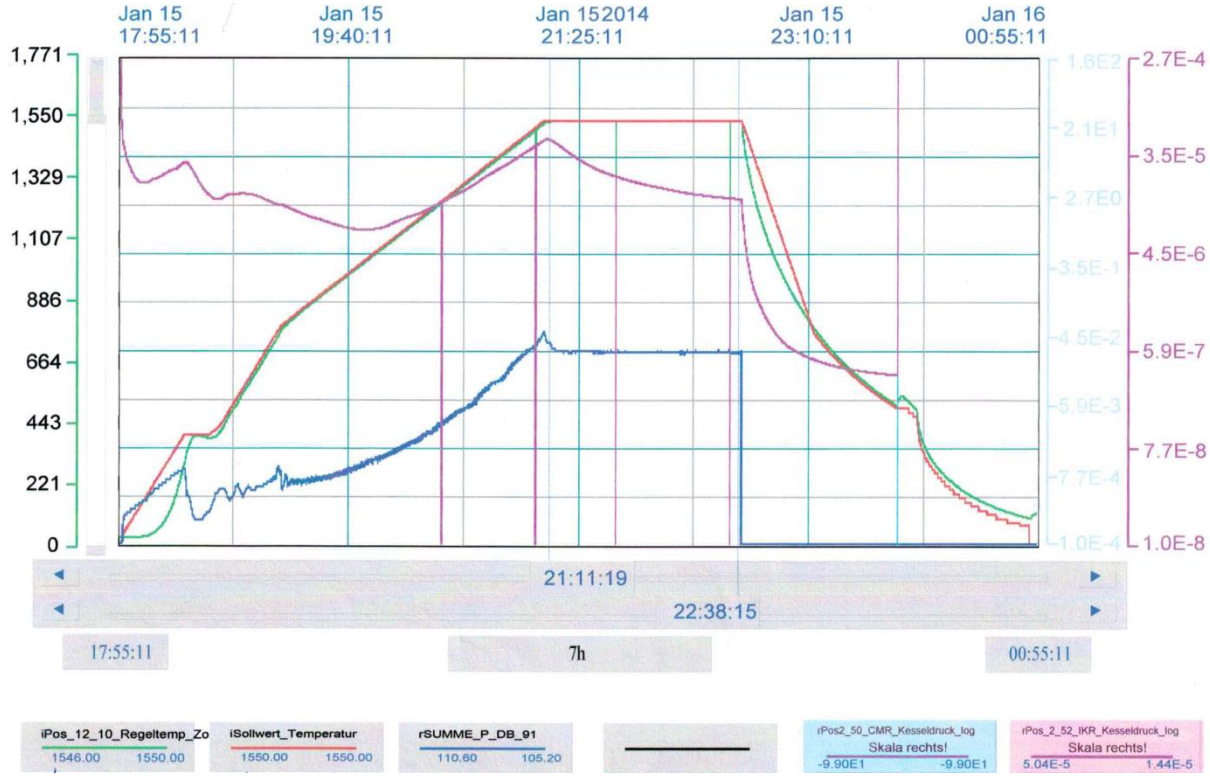

8.5 Weld sample design

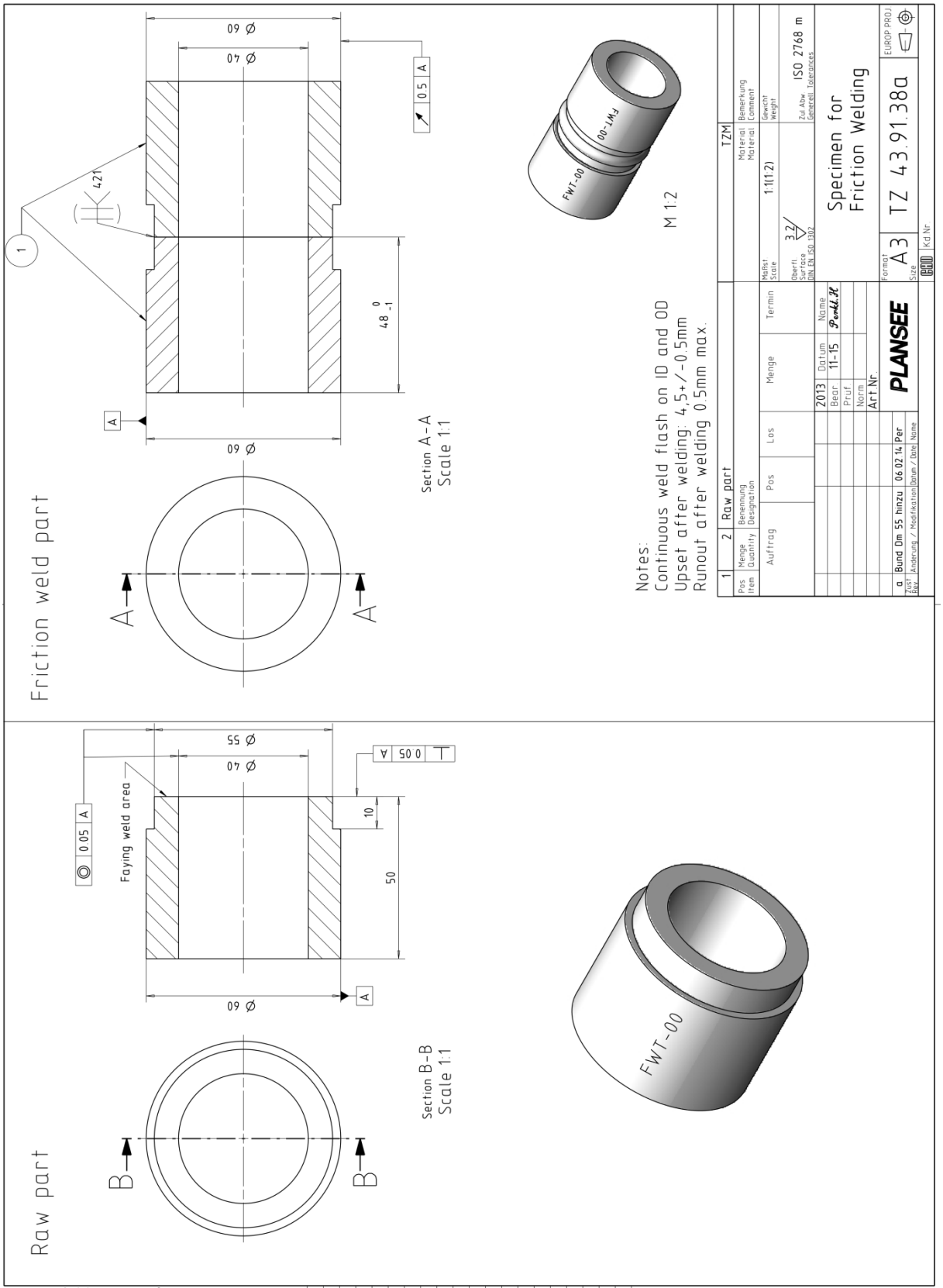

8.6 Tensile sample geometry

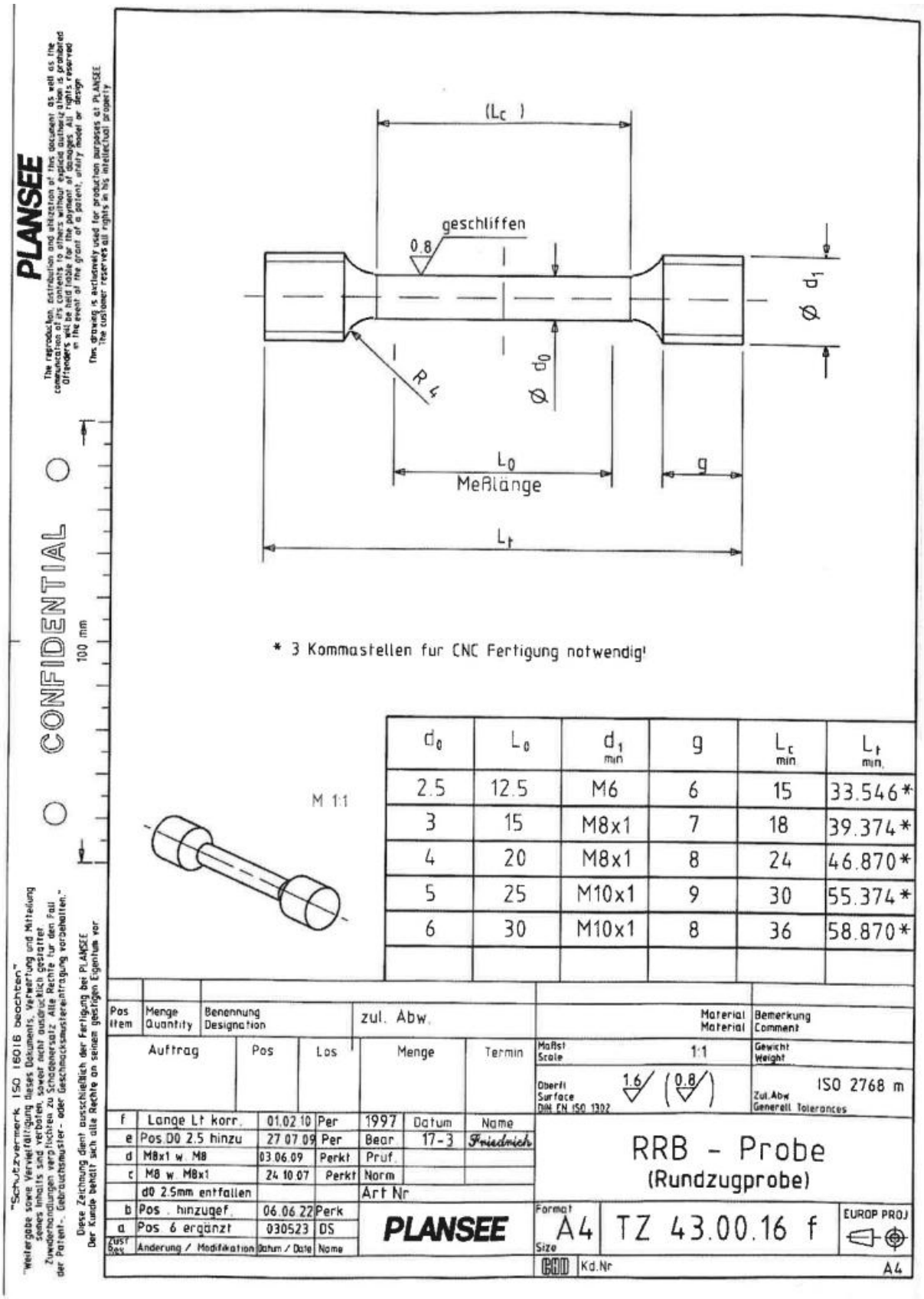

d_0	L_0	d_1 min	g	L_c min	L_t min.
2.5	12.5	M6	6	15	33.546*
3	15	M8x1	7	18	39.374*
4	20	M8x1	8	24	46.870*
5	25	M10x1	9	30	55.374*
6	30	M10x1	8	36	58.870*

Pos Item	Menge Quantity	Benennung Designation	zul. Abw.	Material Material	Bemerkung Comment
	Auftrag	Pos	Los	Menge	Termin

Maßst Scale 1:1 — Gewicht Weight

Oberfl Surface DIN EN ISO 1302 1.6 (0.8) — ISO 2768 m, Zul.Abw Generell Tolerances

Zust Rev	Änderung / Modifikation	Datum / Date	Name
f	Lange Lt korr.	01.02.10	Per
e	Pos.D0 2.5 hinzu	27.07.09	Per
d	M8x1 w. M8	03.06.09	Perkt
c	M8 w. M8x1	24.10.07	Perkt
	d0 2.5mm entfallen		
b	Pos . hinzugef.	06.06.22	Perk
a	Pos 6 ergänzt	030523	DS

1997 Datum Name
Bear 17-3 Friedrich
Pruf.
Norm
Art Nr

PLANSEE

RRB - Probe
(Rundzugprobe)

Format Size A4 — TZ 43.00.16 f — EUROP PROJ

Kd.Nr A4

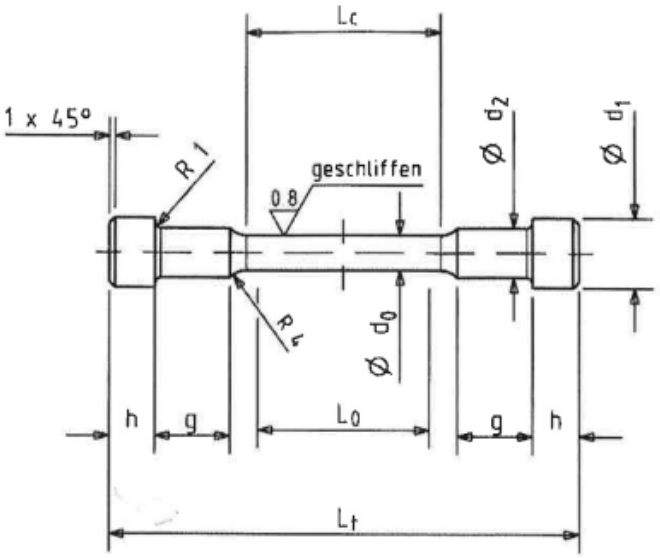

d_0	L_0	d_1 min.	d_2	g	h min.	L_c min.	L_t min.
3	15	7	5	12	6	18	59.292*
4	20	9	6	12	7	24	67.292*
5	25	11	8	12	7	30	74.244*
6	30	12	8.5	12	8	36	81.810*

* 3 Kommastellen für CNC Fertigung notwendig!

"Schutzvermerk ISO 16016 beachten"
"Weitergabe sowie Vervielfältigung dieses Dokuments, Verwertung und Mitteilung seines Inhalts sind verboten, soweit nicht ausdrücklich gestattet. Zuwiderhandlungen verpflichten zu Schadenersatz. Alle Rechte für den Fall der Patent-, Gebrauchsmuster- oder Geschmacksmustereintragung vorbehalten."

Diese Zeichnung dient ausschließlich der Fertigung bei PLANSEE. Der Kunde erhält sich alle Rechte an seinem gestatten Eigentum vor

PLANSEE

The reproduction, distribution and utilization of this document as well as the communication of its contents to others without expressed authorization is prohibited. Offenders will be held liable for the payment of damages. All rights reserved in the event of the grant of a patent, utility model or design.

This drawing is exclusively used for production purposes at PLANSEE. The customer reserves all rights on his intellectual property.

CONFIDENTIAL

100 mm

Pos Item	Menge Quantity	Benennung Designation	zul. Abw.	Material Material	Bemerkung Comment
Auftrag	Pos	Los	Menge / Termin	Maßst. Scale 1:1	Gewicht Weight
				Oberfl. Surface 1.6 (0.8)	Zul. Abw. Generell Tolerances ISO 2768 m

		1996	Datum	Name
		Bear	2-5	Friedrich
		Prüf.		
		Norm		
		Art Nr		

RRS - Probe
(Rundzugprobe)

a	Lange Lt Korr.	01.02.10	Per	PLANSEE
Zust. Rev	Änderung Modification	Datum Date	Name Name	TZ 43.00.11a

Ers f. | ers d. | CAD | Kd Nr | A4 | EUROP PROJ

8.7 Sampling of tensile samples

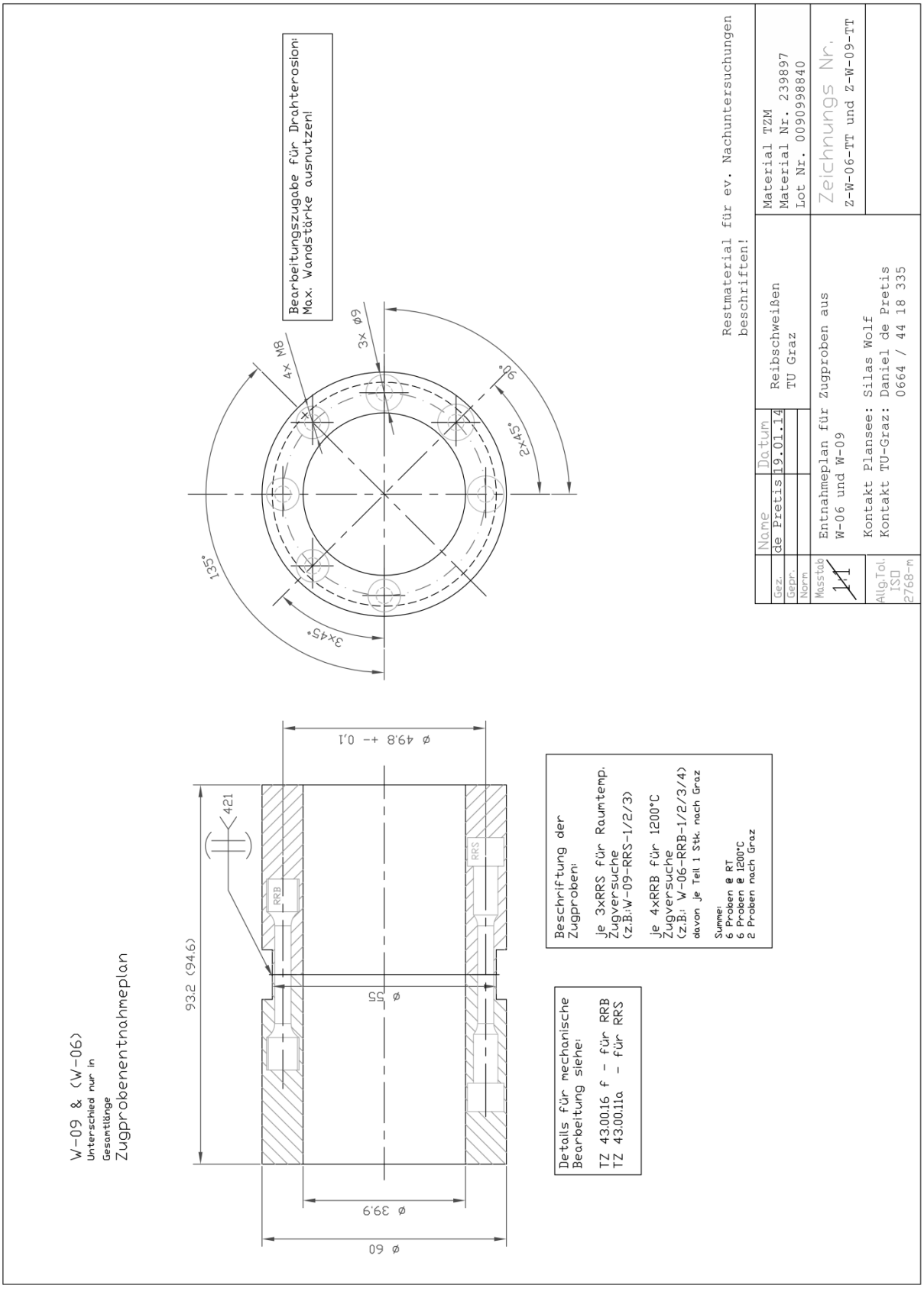

8.8 ASTM grain size measurements

Nr.:	ASTM Nr	Dateiname	ScaleX	ScaleY	Unit	dm Korn	Korn/mm²
1	7	r_mo13u0011.	0,5397	0,5397	µm	0,0313	1024

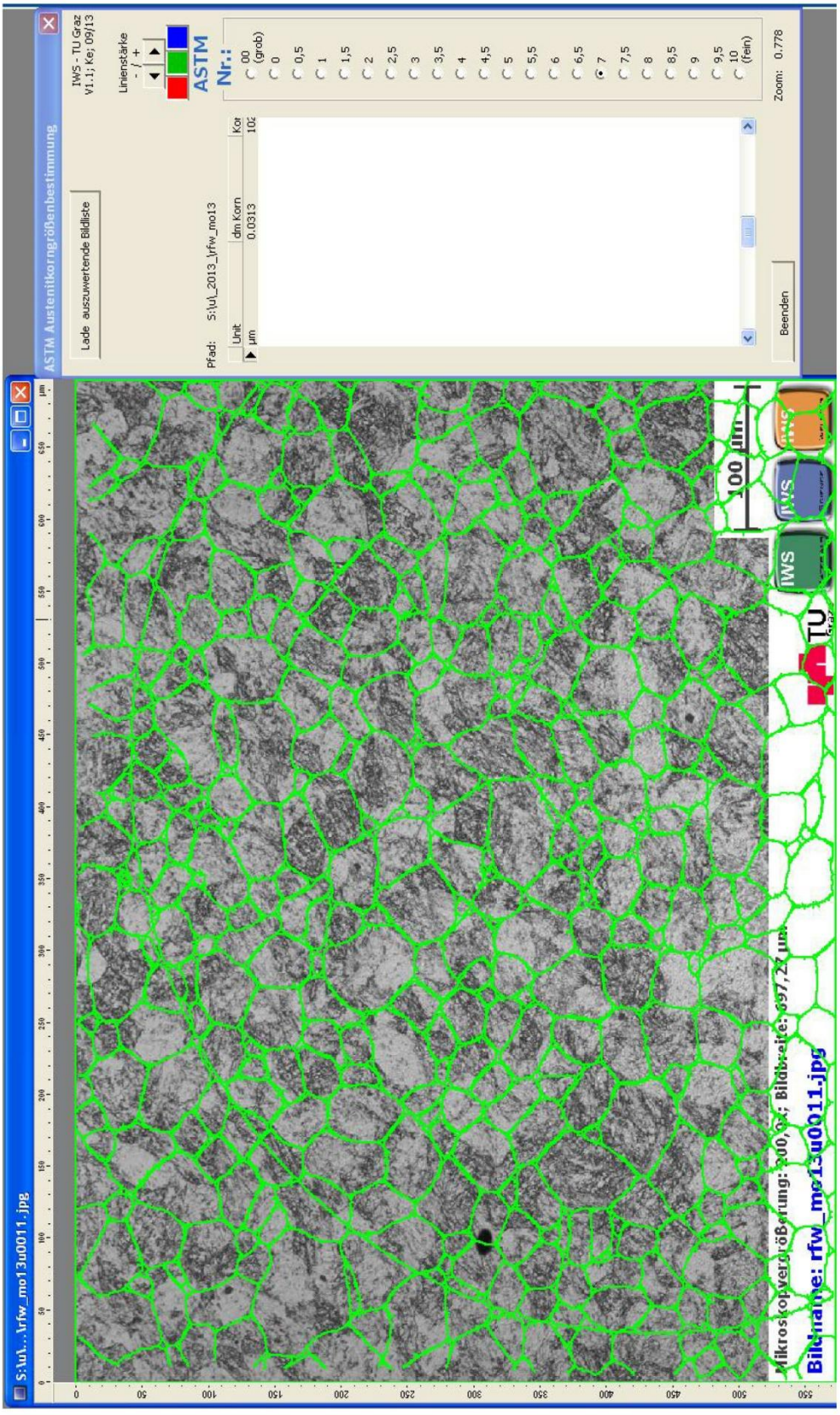

8.9 Macro photos of tensile specimens

Base material high temperature samples Rl2_RRB_1_2_3 **(1= always top sample, 2=middle one, 3=lowest one)**

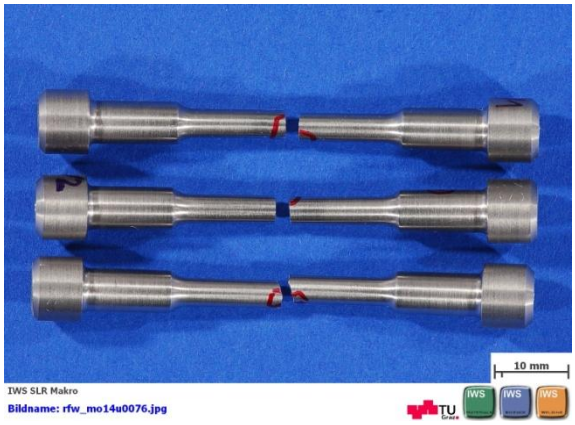

Room temperature samples W06_RRS_1_2_3

Room temperature samples W09_RRS_1_2_3

High temperature sample W06_RRB3

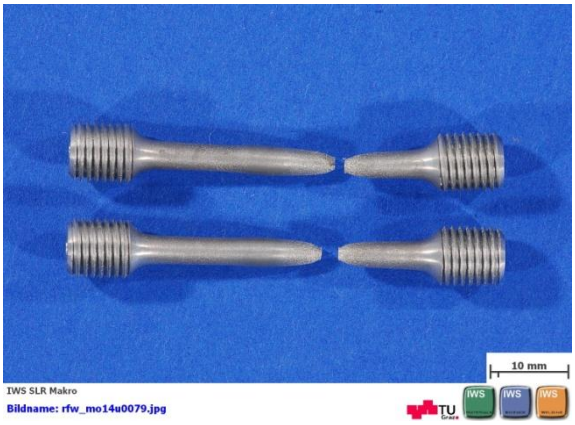

High temperature samples W09_RRB_2_4

8.10 Defect measurement

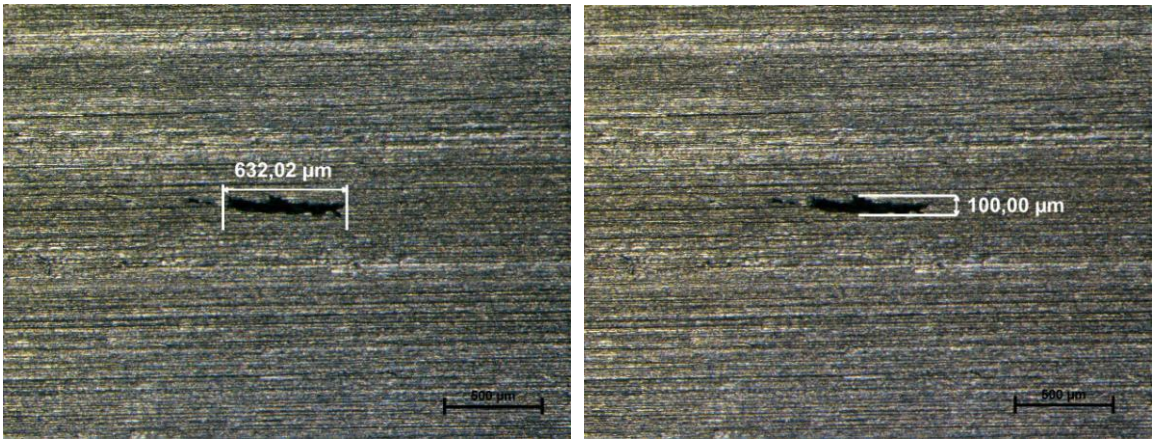

Crack measurements on W-07_UT after flash removal (max. 630x100µm extension)